Evolution of the Atlantic Intertropical Convergence Zone, and the South American and African monsoons over the past 95-Myr and their impact on the tropical rainforests

R. Paul Acosta[1], Jean-Baptiste Ladant[2], Jiang Zhu[3], Christopher J. Poulsen[1]

[1] Earth and Environmental Science Department, University of Michigan, Ann Arbor, Michigan, USA
[2] Laboratoire des Science du Climat et de l'Environnement, LSCE/IPSL, CEA-CNRS-UVSQ, Université Paris-Saclay, 91191 Gif-sur-Yvette, France
[3] Climate and Global Dynamics Laboratory, National Center for Atmospheric Research, Boulder, Colorado, USA

Corresponding author: R. Paul Acosta (acostar@umich.edu)

Key Points:

- Rifting of West Gondwana initiated the Atlantic Intertropical Convergence Zone and altered the South American and African monsoons.
- Simulations of Cenomanian, early Eocene, and middle Miocene indicate paleogeography instead of CO_2 control monsoon distribution.
- Through time, changes in South American and African monsoon circulation influenced the evolution of the Amazon and African rainforests.

This is the author manuscript accepted for publication and has undergone full peer review but has not been through the copyediting, typesetting, pagination and proofreading process, which may lead to differences between this version and the Version of Record. Please cite this article as doi: 10.1029/2021PA004383.

Abstract

The widening of the South Atlantic Basin led to the reorganization of regional atmospheric and oceanic circulations. However, the response of the Atlantic Intertropical Convergence Zone (ITCZ), and South American and African monsoons across paleoclimate states, especially under constant paleogeographic and climatic changes, has not been well understood. Here we report on paleoclimate simulations of the Cenomanian (~95 Ma), early Eocene (~55 Ma), and middle Miocene (~14 Ma) using the Community Earth System Model version 1.2 (CESM1.2) to understand how the migration of the South American and African continents to their modern-day positions, uplift of the Andes and East African Rift Zone, and the decline of atmospheric CO_2 changed the Atlantic ITCZ, and the South American and African monsoons and rainforests.

Our work demonstrates that the South Atlantic widening developed the Atlantic ITCZ. The South Atlantic widening and Andean orogeny led to a stronger South American monsoon. We find the orogeny of the East African Rift Zone is the primary mechanism that strengthened the East African monsoon, whereas the West African monsoon became weaker through time as West Africa migrated toward the subtropics and CO_2 levels fell below 500 ppm. We utilize the Köppen-Geiger Climate Classification as an indicator for maximum rainforest extent. We find that during the Cenomanian and early Eocene, a Pan-African rainforest existed, while the Amazon rainforest was restricted toward the northwestern corner of South America. During the middle Miocene, the Pan-African rainforest was reduced to near its modern-day size, while the Amazon rainforest expanded eastward.

Plain Language Summary

The rifting of the West Gondwana supercontinent from the middle Cretaceous led to the opening of the South Atlantic Basin and the reorganization of regional atmospheric and oceanic circulations. However, the evolution of the South American and African continents under constant paleogeographic and climatic changes has not been well understood. Here we report on paleoclimate simulations since the middle Cretaceous using the Community Earth System Model version 1.2 to understand how the widening of the South Atlantic Basin, uplift of the Andes and East African Rift Zone, and CO_2 decline through time influenced the Atlantic Intertropical Convergence Zone (ITCZ), and the South American and African monsoons and rainforests. Our results suggest that both changes in geography and topography have a first-order control on the

rainfall distribution of the Atlantic ITCZ, South American, and African monsoon. Increased atmospheric CO_2 in the past enhanced tropical precipitation, but it does not determine where it occurs. Our work shows that when the South Atlantic Basin was narrowed, the eastern Amazon rainforest did not exist, while a Pan-African rainforest expanded toward the subtropics. As the South Atlantic Basin widened, the eastern Amazon rainforest formed, while the Pan-African rainforest shrunk to its modern-day size.

Introduction

The seasonal, cross-hemisphere migration of the Atlantic Intertropical Convergence Zone (ITCZ) and its transition into distinct tropical monsoon systems, the South American and the African monsoons, delivers substantial precipitation into the South American and African continents. These atmospheric circulations drive continental hydroclimate and consequently regulate the expansion and contraction of the regional tropical rainforest systems. The ITCZ and monsoons are strongly influenced by the position of the surrounding landmasses (Gill, 1980; Privé & Plumb, 2007b), which differed substantially in the past (Pletsch et al., 2001; Seton et al., 2012). For example, based on paleoclimate simulations of the late Paleozoic and early Mesozoic (~250 Ma), when the South American and African continents was the West Gondwana mega-continent, a single "mega-monsoon" system determined the hydrological cycle (Kutzbach & Gallimore, 1989; Peyser & Poulsen, 2008). Understanding the transition from the Gondwana "mega-monsoon" circulation toward the modern Atlantic ITCZ and monsoon systems can shed light on the evolution of the South American and African hydroclimate systems. Additionally, as the South American and African continents migrated toward their modern-day positions, regional topography and climate were also in flux, further adding complexity to the system. Our work aims to disentangle the role of continental drift, orography, and CO_2, as the modern-day Atlantic ITCZ and South American and African monsoons evolved through time. In doing so, we can then discuss how the evolution of the regional hydroclimate system shaped Amazonian and African rainforests.

The ITCZ is part of the tropical ascending branch of the Northern and Southern Hemisphere Hadley Cells circulations coinciding with regions of maximum sea surface temperatures (SSTs). The strong low-level (~850 mb) convergence via tropical easterly winds feeds moisture to tropical convective systems and produces a substantial amount of rainfall

(Geen et al., 2020). Today, the Atlantic ITCZ seasonally migrates between 10°N (boreal summer) and 10°S (austral summer) and brings rain to the eastern coast of South America and the coast of West Africa. Meanwhile, continental monsoon systems are seasonal off-equatorial displaced rising branches of the Hadley cell, associated with seasonal precipitation and wind reversals (Gadgil, 2018). The South American monsoon extends down to 30°S during the austral summer months (December-February; DJF). Precipitation from the South American monsoon enables the modern Amazon rainforest to span the entire northern half of South America and terminates at ~10°S (Peel et al., 2007). The African monsoon is typically divided into several distinct monsoon regimes, the West African monsoon, which extends northward to 15°N during boreal summer months (June-August; JJA), and the East African monsoon that reaches southward to 15°S during austral summer months (Battisti et al., 2018; Geen et al., 2020) and the Central African monsoon as a transitionary circulation between the East and West African monsoons (Farnsworth et al., 2011). The African monsoons enable the African rainforest to extend from 5°N to 5°S (Peel et al., 2007). However, through time, changes in South American and African paleogeography, the position of landmasses, and topographies most likely modified the surface and upper-level thermodynamic structure of the atmosphere and Atlantic Ocean circulation, which could have altered the Atlantic ITCZ and the South American and African monsoons.

The rifting of the Gondwana mega-continent initiated paleogeographic changes leading to the present-day configuration (Ziegler et al., 2003). The cleaving of South America and Africa began in the early Jurassic (~200 Ma) and lasted through the early Cretaceous (~145 Ma) (Moulin et al., 2010; Seton et al., 2012). A shallow marine corridor first appeared around the middle Cretaceous (~100 Ma) and formed a narrow South Atlantic Basin, which widened through the Cenozoic (Pletsch et al., 2001). Additionally, the African plate experienced counterclockwise rotation and northwestward movement, while the South American plate moved northeastward (Seton et al., 2012). As the South American and the African continents moved to their modern-day positions, orogens formed that likely further shaped the hydroclimate on the continents. The South American Andes (Boschman, 2021; Garzione et al., 2017; Lossada et al., 2017) and East African Rift System (Jess et al., 2020; Roberts et al., 2012; Wichura et al., 2015) are thought to have reached modern elevations between the early Eocene (~33 Ma) and late Miocene (~7 Ma). Proxy (Garzione et al., 2017; Hoorn et al., 2010) and modeling (Carrapa et al.,

2019; Poulsen et al., 2010) evidence suggest that the South American monsoon was strengthened during the Neogene (~20 Ma), coinciding with the uplift of the Andes. Similar evidence (Jung et al., 2016; Hans Peter Linder, 2017; Sepulchre et al., 2006) suggests that the uplift of the East Africa Rift System strengthened the East African monsoon system (Ogwang et al., 2014).

Over the past 95-Myr, in addition to paleogeographic changes, global atmospheric CO_2 levels fluctuated from more than 1000 ppm during the late Cretaceous and the Paleocene-Eocene boundary (95-55 Ma) (Foster et al., 2017) to well below 400 ppm during the late Miocene (~10 Ma) (Beerling & Royer, 2011). Fluctuation in CO_2 levels is thought to drive the global climatic variability (Foster et al., 2017; Tierney et al., 2020), influencing surface temperatures and the hydrological cycle (Anagnostou et al., 2016; Gaskell et al., 2022). Warmer conditions increase the amount of available atmospheric water vapor relative to the amount precipitated back to the surface (Held & Soden, 2006), suggesting wet regions could have experienced higher precipitation rates while already arid regions could have experienced higher evaporation rates, particularly over the subtropical regions (Scheff et al., 2017). Additionally, a reduced meridional temperature gradient is hypothesized to weaken the Hadley cell overturning circulation (Frierson et al., 2007; Held & Soden, 2006). Such weaker surface wind convergence toward the tropics is hypothesized to produce more in situ precipitation in the subtropics (N. J. Burls & Fedorov, 2017). This previous work suggests that higher CO_2 levels in the past could have led to more subtropical precipitation and perhaps an expansion of tropical rainforest biomes.

The Gondwana breakup changed the strength and locality of the Atlantic ITCZ and South American and African monsoon systems and likely impacted the regional ecosystem. For example, previous paleoclimate simulations of the South American and African monsoon of the late Cretaceous (A. B. G. Bush & Philander, 1997; Ohba & Ueda, 2010), early Eocene (M. Huber & Goldner, 2012), middle Miocene (Herold et al., 2011), and modern-day (Liu et al., 2019) show a weak Atlantic ITCZ when the South Atlantic Basin was narrow, but overall persistent South American and African monsoons. In support, proxy evidence (Ziegler et al., 2003) suggests the environment over northwest South America and East Africa was dominated by evergreen forests (Morley, 2011). In contrast, pronounced seasonality in rainfall over equatorial Africa suggests the existence of a swamp-like versus tropical rainforest environments. Plant fossil records from the Colombia and Venezuela region indicate that the Amazon rainforest was already established in the northwestern part of South America by the Maastrichtian period

(~70 Ma), with species richness peaking during the middle Eocene (~40 Ma) and attaining greater plant diversity than the modern-day Amazon rainforest (Jaramillo et al., 2010). Such an increase in plant diversity has been linked to increased global temperature during the early Cenozoic, when CO_2 levels were well above 1000 ppm (Beerling & Royer, 2011; Morley, 2011). Meanwhile, a "Pan-African" rainforest is thought to have spanned the width of the African continent and well into the subtropics, with its peak also occurring during the warm house climate of the Cenomanian and the Paleocene-Eocene period (Couvreur et al., 2021). In support, records of angiosperm pollen show an increase in plant species diversity in both South America and Africa during the early Eocene (~55 Ma) (H. Peter Linder, 2014; Hans Peter Linder, 2017).

As CO_2 declined in the middle-to-late Eocene (~38 Ma), records suggest species richness decreased in South America and Africa. However, the South American rainforest system experienced a rebound in species richness during the Neogene, while the African rainforests continued declining (Morley, 2011). Sedimentary records from the Amazon river network suggest that a "Pan-Amazonian" rainforest—spanning across the entirety of northern South America and extending well into the subtropics (30°S)—existed in the late Miocene (~7 Ma) during times when CO_2 levels were much lower, and the climate system was much cooler than the early Cenozoic (Hoorn et al., 2010; Lundberg et al., 1998). The east and southward expansion of the Amazon rainforest with the simultaneous decline of the African rainforest implies that the decrease in global atmospheric CO_2 and associated climatic changes cannot fully explain the regional vegetation changes between the two continents. While much of the literature highlights the role of Andean orography as the dominant mechanism that strengthens the South American monsoon during the Neogene (Garzione et al., 2017), the role of widening of the South Atlantic Basin (Liu et al., 2019; Ziegler et al., 2003) has been suggested as an additional mechanism that can enhance the South American monsoon.

To understand the role of continental drift, orography, and CO_2 on the hydroclimate system of South America and Africa, we present a systematic analysis of the evolution of the Atlantic ITCZ, South American, and African monsoon circulations over the last 95-Myr. Here, we use time-specific paleogeographic reconstructions of the late Cretaceous (Cenomanian, ~95 Ma), early Eocene (~55 Ma), middle Miocene (~15 Ma), and the preindustrial. We then discuss how changes in paleogeography and CO_2 impacted the South American and African rainforests.

2 Method

2.1 Model

We use the National Center for Atmospheric Research general circulation model (GCM), Community Earth System Model version 1.2 (CESM1.2) (Meehl et al., 2013), a fully coupled global climate model that is equipped with atmosphere, land, river, ocean, and sea-ice components. Specifically, CESM1.2 comprises the Community Atmospheric Model version 5 (CAM5) (Neale et al., 2010), Community Land Model version 4.5 (Oleson et al., 2013), Sea Ice model (Hunke, 2010), Parallel Ocean Program version 2 (Danabasoglu et al., 2012) and a river transport model (Oleson et al., 2013). The simulations were carried out with the finite volume dynamical core version of the atmosphere model with a grid spacing of 1.9° × 2.5° equal to ~200 km over the equator. Ocean and sea ice models have a nominal 1° resolution.

2.2 Experiments and Boundary conditions

Four primary CESM1.2 simulations were performed as part of this study. Each was run with age-specific paleogeography and land-surface conditions. Most other boundary conditions were specified with preindustrial values, except as noted, to minimize non-geography-related differences. Our preindustrial (PI) simulation is utilized as the modern-day analog. We perform simulations of the middle Miocene, early Eocene, and Cenomanian periods with multiple atmospheric CO_2 levels. To isolate the role of paleogeography, our analysis primarily focuses on the simulations with preindustrial level CO_2 (~280 ppm). Simulations with higher time-specific CO_2 levels (400 ppm for the middle Miocene, 1700 ppm for the early Eocene, and 1700 ppm for the Cenomanian) are briefly touched upon. The selected CO_2 levels for the high-CO_2 simulations were based on previous model-data studies (N. J. Burls et al., 2021; A. Goldner et al., 2014; Lunt et al., 2017; C. R. Tabor et al., 2016; Zhu et al., 2019). The middle Miocene, early Eocene, and Cenomanian simulations were run for at least 1500 years to bring the surface climate into steady-state and have a top of the atmosphere energy imbalanced of no more than 0.3 (W/m2). Full equilibration of the deep oceans would likely require several thousand years of additional integration. For detailed information regarding the integration length of simulations and assessment of the equilibrium state, readers are referred to supplementary table 1 [see also *Goldner et al.*, 2014; *Zhu et al.*, 2019].

The progressive widening of the South Atlantic Basin, northwest movement of the South American continent, and northeast movement of the African continent from the late Cretaceous to the modern-day is illustrated in Figure 1. The width of the South Atlantic Basin at 10°S (Fig. 2a) was approximately 25%, 50%, and 90% of the PI value during the Cenomanian, early Eocene, and middle Miocene. The boundary conditions include substantial differences in paleotopography that are shown in figure 1 and highlighted in table 1. We elaborate on the specific paleoclimate boundary conditions below. For the global paleogeographic distribution, see supplementary figure S1.

The middle Miocene simulations (MIO) in this study used the boundary conditions that were initialized from the high ice sheet, 400 ppm pCO_2 middle Miocene Climatic Optimum simulation in Goldner et al. (2014), and were published in Gaskell et al. (2022). Unlike CCSM4 in Goldner et al. (2014), we used CESM1.2, which has an updated atmosphere model CAM5 and has been demonstrated to have improved performance for paleoclimate simulations (Zhu et al., 2020). The South American and African vegetation represents tropical moist environmental conditions and is dominated by tropical and temperate forests with grasslands (Fig. S4; Herold et al., 2010). The aerosol prescription was specified as the preindustrial natural aerosol distribution. The simulations use a set of preindustrial orbital parameters with a fixed solar forcing for 1850 AD.

The early Eocene simulations were from the published work of *Zhu et al.* (2019), which used the published topography and bathymetry boundary conditions of the early Eocene (~55 Ma) (Herold et al., 2014; Lunt et al., 2017). South American and African continents consist of a warm and dry vegetation biome with shrubland and desert-dominated ecosystems. The northwest sector of South America and significant parts of the African continent along the equatorial region possess some tropical rainforests but are dominated by shrubland and grassland (Fig. S2; Herold et al., 2014). Preindustrial natural aerosols prescriptions were redistributed based on the Eocene paleogeography following the method of *Heavens et al.* [2012]. In this method, the Modal Aerosol Model is used to simulate a prognostic sea salt and dust aerosol distribution based on topography, bathymetry, and land information (vegetation and glaciation). Aerosols such as dimethylsulfide and black carbon were distributed symmetrically between hemispheres using monthly zonal average preindustrial values.

The Cenomanian (~95 Ma) simulations used for this study are revised versions from the recently published Community Climate System Model version 4 (CCSM4), Cenomanian simulations (Ladant et al., 2020; C. R. Tabor et al., 2016). The Cenomanian boundary conditions are from the proprietary Getech Plc based paleogeography (Lunt et al., 2016; C. R. Tabor et al., 2016). We update the CCSM4 Cenomanian simulations using the CESM1.2. Like the Eocene CESM1.2 simulations, aerosols reconstructions use the *Heavens et al.*, [2012] method. The vegetation distribution in South American and African continents consists of a temperate forest in the tropics but is dominated by shrubland and grassland (Fig. S2; (Sewall et al., 2007). The Cenomanian simulation accounted for the ~1% decrease in solar irradiance (Ladant et al., 2020), which have been shown to decrease the global mean temperature by 1.8°C (Laugié et al., 2020).

Table 1. Model Experiments

Case Name	Ocean Configuration	CO_2 (ppm)	Dominant South America and Africa vegetation Type	Aerosols	Miscellaneous
PI	Fully Coupled	284.7	Preindustrial	Preindustrial	Simulation from Zhu et al., 2019
MIO.280	Fully Coupled	280	Tropical and evergreen forest Herold et al., 2010	Preindustrial	Boundary Conditions from Goldner et al., 2014 ran with CESM1.2 CAM5
MIO.400	Fully Coupled	400	Tropical and evergreen forest Herold et al., 2010	Preindustrial	Boundary Conditions from Goldner et al., 2014
MIO.280.FLAT	Fixed SST	280	Tropical and evergreen forest Herold et al., 2010	Preindustrial	Branched from MIO.280 with South American and African terrain set to 100 meters
MIO.280.Sav	Fully Coupled	280	Savannah	Preindustrial	Branched from MIO.280 with South American and African vegetation set to savannah
EOC.280	Fully Coupled	280	Dry shrubland and desert dominated with small clusters of tropical forest Herold et al., 2014.	Heavens et al. 2012	Simulation from Zhu et al., 2019
EOC.1700	Fully Coupled	1700	Dry shrubland and desert dominated with small clusters of tropical forest Herold et al., 2014.	Heavens et al. 2012	Simulation from Zhu et al., 2019
EOC.280.FLAT	Fixed SST	280	Dry shrubland and desert dominated with small clusters of tropical forest Herold et al., 2014.	Heavens et al. 2012	Branched from EOC.280 with South American and African terrain set to 100 meters
EOC.280.SST	Fixed SST	280	Dry shrubland and desert dominated with small clusters of tropical forest Herold et al., 2014.	Heavens et al. 2012	Branched from EOC.280 with $2°C$ added to SSTs

					found over west equatorial Atlantic Basin
EOC.280 Sav	Fully Coupled	280	Savannah	Heavens et al. 2012	Branched from EOC.280 with South American and African vegetation set to savannah
CEN.280	Fully Coupled	280	Low latitude forest and dominated by shrubland and savannah Sewall et al., 2007	Heavens et al. 2012	Boundary conditions from Ladant et al., 2020 ran with CESM1.2 CAM5
CEN.1700	Fully Coupled	1700	Low latitude forest and dominated by shrubland and savannah Sewall et al., 2007	Heavens et al. 2012	Boundary conditions from Ladant et al., 2020 ran with CESM1.2 CAM5
CEN.280.FLAT	Fixed SST	280	Low latitude forest and dominated by shrubland and savannah Sewall et al., 2007	Heavens et al. 2012	Branched from CEN.280 with South American and African terrain set to 100 meters

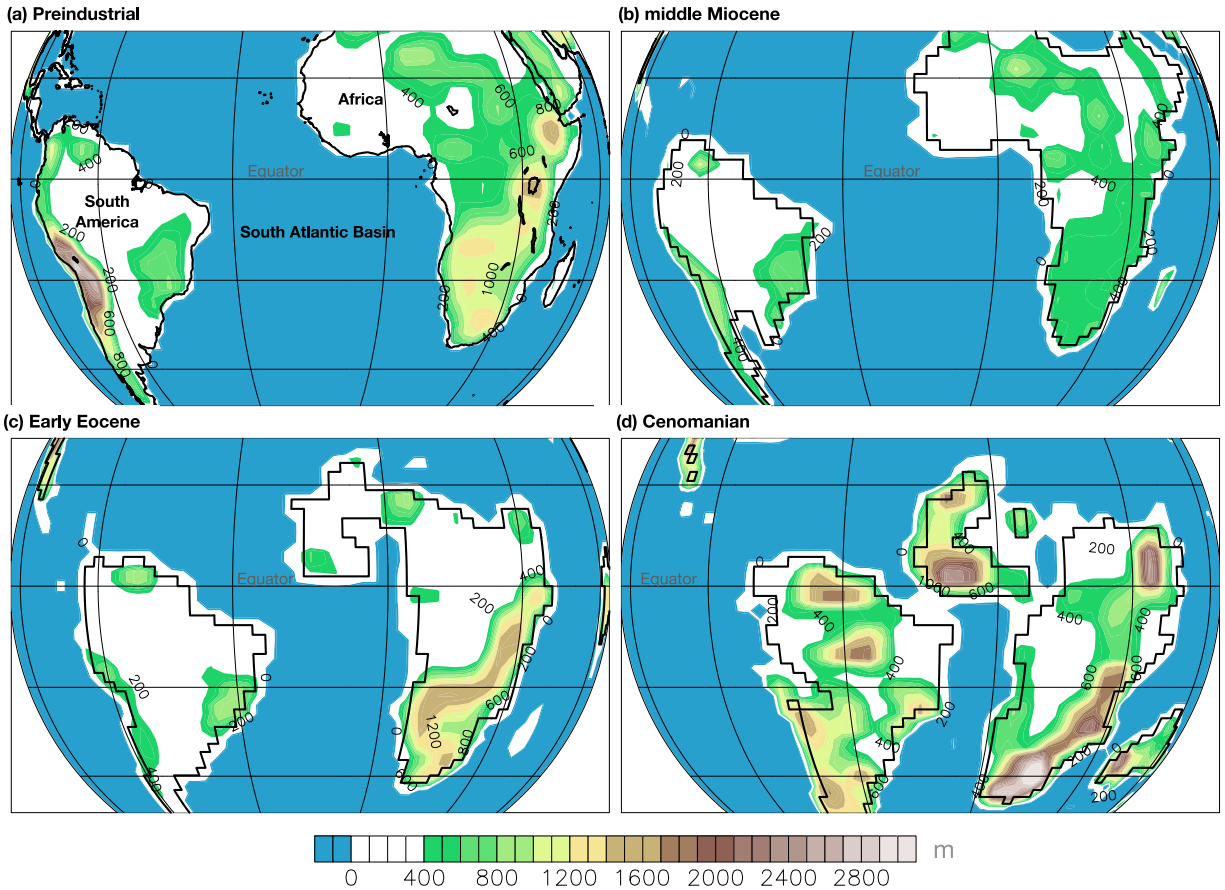

Figure 1. South American and African geography and topography (m) for (a) Preindustrial, (b) middle Miocene (~15 Ma), (c) early Eocene (~55 Ma), and (d) Cenomanian (~90 Ma) simulations.

2.3 Diagnostics, Sensitivity Studies, and Limitations

2.3.1 Intertropical Convergence Zone and Monsoon Diagnostics

The ITCZ is typically defined as a band of enhanced tropical convection and precipitation within the axisymmetric overturning circulation of the Northern and Southern Hemisphere Hadley cells where northerly and southerly trade winds converge over the ocean (Geen et al., 2020). Away from the equator, monsoon circulation develops as maximum solar insolation seasonally migrates between hemispheres, resulting in the maximum moist static energy to be located off the equator and a switch from an axisymmetric to an asymmetric overturning circulation (Gadgil, 2018; Privé & Plumb, 2007a). Aside from total precipitation, this study uses the quasi-convective equilibrium framework (Nie et al., 2010) to help identify changes in Atlantic ITCZ, South American, and African monsoon circulations. In this view, regions of deep convection and large-scale ascent cause the atmosphere thermodynamic profile to approach the moist adiabat. ITCZ and monsoon convective regions are identified by the coupling of subcloud (~850 mb) and upper-level (~200 mb) equivalent potential temperature (θ_e) (Nie et al., 2010) and designates as the region with maximum moist static energy. In addition, total diabatic heating is used to represent precipitation occurring in the atmospheric column and help identify large-scale atmospheric ascent (Wright & Fueglistaler, 2013). Total precipitable water and moisture flux are utilized to identify changes in the atmospheric hydrological cycle. We focus on subcloud θ_e and sea surface temperature (SST) distribution to determine the impact of changing paleogeography on the Atlantic ITCZ, South American, and African monsoons. However, aside from the location of maximum subcloud θ_e, an ITCZ versus monsoon induced convective systems are indistinguishable thus we provide vertical profile analysis of the Hadley cell overturning circulation to further analyze changes in the ITCZ circulation (Fig. 2) and we supplement the thermodynamic framework presented in our results with a simplified modern-day monsoon index (Carmichael et al., 2016; Wang & Ding, 2006) to further identify monsoon regions in our paleoclimate simulations (Fig. S13).

2.3.2 Köppen-Geiger Climate Classification

In lieu of a dynamic vegetation model, to quantify changes in the South American and African tropical rainforest extent between the middle Miocene, early Eocene, and Cenomanian, we use the Köppen-Geiger Climate Classification (referred to as KGCC hereafter) (Peel et al., 2007). In

KGCC, a tropical rainforest, monsoon, and savannah all maintain temperatures above $18°C$ during the coldest month (T_{cold}). These three ecosystems are distinguished by their dry month precipitation (P_{dry}): tropical rainforest has greater than 60 mm, monsoon vegetation has rates less than 60 mm but greater than or equal to 100 minus (mean annual precipitation/25), and savannah has P_{dry} less than 60 mm and 100 minus (mean annual precipitation/25).

2.3.3 Additional sensitivity Studies

We offer complimentary low-CO_2 (280 ppm) fixed SST simulations to explore the sensitivity of our results to orography, coastal SST warming, and vegetation distribution. To understand the role of orography, we performed fixed SST simulations in which the South American and African terrains were set to 100 meters (Fig. S4 and S5). We highlight the impact of changes in SST distribution on the Atlantic ITCZ and South American monsoon, using a fixed SST simulation of the early Eocene where the northeastern coast of South America was warmed by 2°C (Fig. S9). We added $2°C$ warming to the northeastern coast to replicate the coastal warming found in the observations, PI, and middle Miocene simulations (Fig. 7a, 7b, and 7c). Finally, since the vegetation distribution in our simulations was prescribed, we use fully coupled simulations to test if modifying the South American and African vegetation would impact the South American and African monsoon precipitation distribution. A set of middle Miocene and early Eocene vegetation sensitivity tests were performed where the ecosystem over South America and Africa were set to savannah grassland type (Fig. S10 and S11). A savannah-type ecosystem should represent a generic vegetation type that does not substantially change the surface albedo compared with an entirely bare ground (desert) or introduce excess evapotranspiration as a fully forested region. We note that fixed SST sensitivity studies used quasi-spun-up SSTs taken from each low-CO_2 fully coupled paleoclimate simulation: MIO.280, ECO.280, and CEN.280.

2.3.4 Limitations

We acknowledge several limitations in our work. Paleogeographic reconstruction of the middle Miocene and early Eocene were based on Müller et al. (2008), while the Cenomanian was based on Markwick & Valdes (2004), which do not use the same reference frames. This lack of self-consistency in plate rotations and paleotopographies, especially between the transition from the

Cenomanian to the early Eocene simulation, represents a degree of uncertainty associated with paleoaltimetry and paleocoastlines (N. J. Burls et al., 2021; Carmichael et al., 2016; Lunt et al., 2017), and should be further tested in the future as better-constrained paleoclimate reconstructions become available. Nonetheless, for the purpose of our work, we find the expansion of the South Atlantic seafloor to be generally consistent with a progressively widening basin and should not substantially alter our findings. Additionally, our study uses prescribed vegetation rather than an interactive vegetation model (Fisher et al., 2015), which lacks the ability to predict the rapid collapse of plant biomes. Recent work (C. Tabor et al., 2020) has shown that the addition of grassland or low albedo plant functional types in northern Africa can also increase the northern extent of the African monsoon and impact the precipitation magnitude of the South American monsoon. The sensitivity of the South American and African climate to prescribed vegetation is explored in supplementary figures S10 and S11. We also note that differences in orbital forcing (Cruz et al., 2009; A. Goldner et al., 2014), land-ice distributions (A. Goldner et al., 2013; Singh et al., 2016), and paleo aerosol distribution (Heavens et al., 2012; Zhu et al., 2019) can also impose forcings on the climate system which were not explored in our study.

3 Results

3.1 Simulation of modern-day tropical precipitation patterns

To assess how well the CESM1.2 captures the Atlantic ITCZ, South American, and African monsoons, we compare precipitation rates in the PI simulation to satellite observations TRMM (Huffman et al., 2007). The TRMM is based on 12 years of climatology from 1998-to 2009. To simplify our comparison in this section, we define the Atlantic ITCZ as an enhanced zonal precipitation band over the ocean that seasonally migrates between the Northern and Southern Hemisphere subtropical Atlantic Basin or ~10° of the equator, while monsoon centers are designated as the location of maximum seasonal precipitation rate over the continent (Fig. 2; Geen et al., 2020). The monthly progression of the South American, West African, and East African monsoons are shown as monthly averaged precipitation rates over the boxed regions in Figure 2 (Fig. 3).

The comparison between TRMM and PI shows that the PI captures the annual distribution of the Atlantic ITCZ and its seasonal cross hemisphere migration (Fig. 2a and 2b).

The PI simulation exhibits a double Atlantic ITCZ pattern (Siongco et al., 2015) during the austral summer but not during the boreal summer. Nonetheless, it captures enhanced precipitation rates along the North Atlantic Basin (Fig. 2f, 2g, 2k, and 2l). High South American monsoon precipitation rates over the Amazon Basin and orographic precipitation along the front of the Andes are captured by the PI (Fig. 2f and 2g). The monthly progression of the South American monsoon in the PI shows a good comparison with TRMM (Fig. 3a, lines grey and black). The maximum East African monsoon precipitation location in the PI and TRMM is at ~18°S (Fig. 2f and 2g). Compared to TRMM, the monthly progression of the East African monsoon precipitation is well captured by the PI simulation but simulates higher austral summer precipitation rates (Fig. 3b, lines grey and black). Compared to TRMM, the PI captures the coastal West African monsoon precipitation but has weaker precipitation rates over central Africa (Fig. 2k and 2l). The monthly progression of the West African monsoon is well captured by the PI but shows greater precipitation rates during the peak boreal summer month of July (Fig. 3c, lines grey and black). The precipitation comparison between PI and TRMM indicates that CESM1.2 does a reasonable job of capturing the modern-day Atlantic ITCZ, South American, and African monsoons and gives confidence to our paleoclimate simulations.

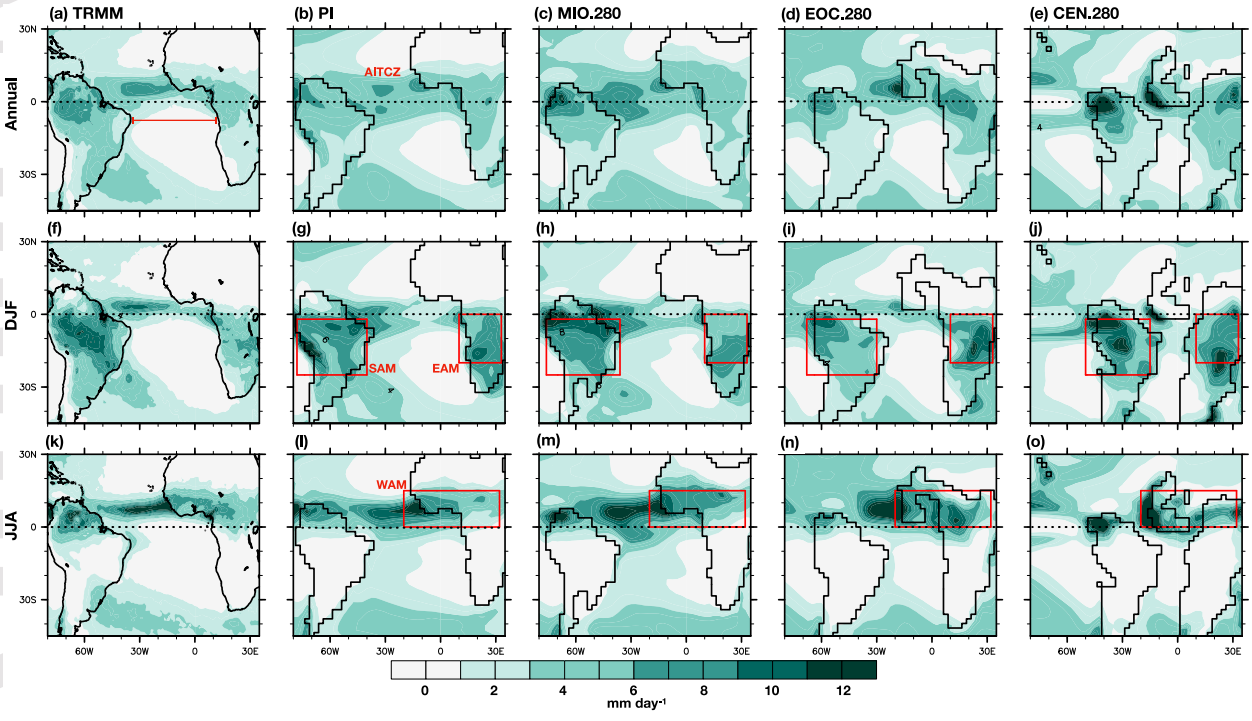

Figure 2. Total precipitation rate (mm day^{-1}) for TRMM (a, f, and k), PI (b, g, and l), MIO.280 (c, h, and m), EOC.280 (d, i, and n), and CEN.280 (e, j, and o). The top row displays the annual mean, the middle row shows the austral summer (DJF), and the bottom row shows the boreal summer (JJA) climatologies. The dashed line represents the equatorial line. The red line across plot (a) represents the longitudinal width across the South Atlantic Basin, where we measured the distance between the South American and African continents. Boxed regions in plots (f) and (k) show the South American (SAM), East African (EAM), and West African (WAM) monsoons regions used for figure 3.

3.2 Simulation of tropical precipitation patterns since the Cenomanian

Since the Atlantic Basin was nearly closed in CEN.280 simulation, much of the Atlantic ITCZ precipitation does not exist (see also analysis in Section 3.3.1). Most of the precipitation occurs along the western coast of Africa or within the continental interior of South America and Africa (Fig. 2e, 2j, 2o). In the EOC.280 simulation, weak precipitation occurs over the Northern Hemisphere Atlantic Ocean, associated with the emergence of the Atlantic ITCZ. However, unlike the PI and TRMM, where the precipitation maximum occurs near the eastern coast of South America, the Atlantic ITCZ during the early Eocene is shifted toward the West African coastline (Fig. 2d, 2l, and 2n), suggesting that the narrow South Atlantic Basin and the southward location of the African continent during the early Eocene strongly influence its location (see Section 3.3). The Atlantic ITCZ fully forms as the South Atlantic Basin is widened in the MIO.280 simulation. Similar to the PI and TRMM, enhanced precipitation over the eastern coast of South America occurs during the austral summer season (Fig. 2h).

The South American monsoon precipitation season duration is approximately the same between the EOC.280, MIO.280, and PI simulations (Fig. 3a), while enhanced precipitation rates occur well into the late spring in the CEN.280 simulation extends. In the CEN.280 and EOC.280 simulations, the South American monsoon is centered over the western coast of South America and exhibits lower precipitation over the eastern Amazon Basin than the PI and TRMM (Fig. 2i and 2j). Similar to the PI, the MIO.280 exhibits enhanced precipitation over the east Amazon Basin and the eastern coastal region (Fig. 2g and 2h). The lack of precipitation over the east Amazon in the simulations when the basin was narrow suggests that the South American monsoon expanded eastward during the late Cenozoic. We further investigate the reason for this expansion in the subsequent section (see Section 3.3.2). However, regardless of the changes in paleogeography, the modern-day monsoon index suggests that in all three periods, the South

American Monsoon brings more than 60% of the annual precipitation over the South American continent and 90% percent over the Amazon region (Fig. S13).

In our simulations, the West African monsoon migrates from near the equator (~1°N) in the Cenomanian to the subtropics (~10°N) in the preindustrial. In both the CEN.280 and EOC.280 simulations, boreal precipitation rates are much greater than in the MIO.280, PI, and TRMM cases (Fig 3c). In the paleoclimate simulations, the West African monsoon has an earlier onset around April and diminishes during the end of the boreal summer (Fig. 3c). In the MIO.280 case, the West African monsoon circulation is much weaker in magnitude and is stretched east-west across the tropical Atlantic Basin and is similar to those found in the PI case suggesting that the West African monsoon weakened through time (see Section 3.3.3 for further analysis). Regardless of the northward shift of the West African monsoon center, the modern-day monsoon index suggests that the West African Monsoon brings more than 60% of the annual precipitation over the North African continent (Fig. S17). In all three paleoclimate cases, the East African monsoon resides near 15°S and is stronger during the early Eocene and Cenomanian. The modern-day monsoon index suggests that in all three periods, the East African Monsoon brings more than 60% of the annual precipitation over the South African continent (Fig. S13). Since the East African monsoon location remains relatively stationary between our paleoclimate simulations but does change in magnitude, we suspect that different topographic configurations could influence our results (see Section 3.5 for further analysis).

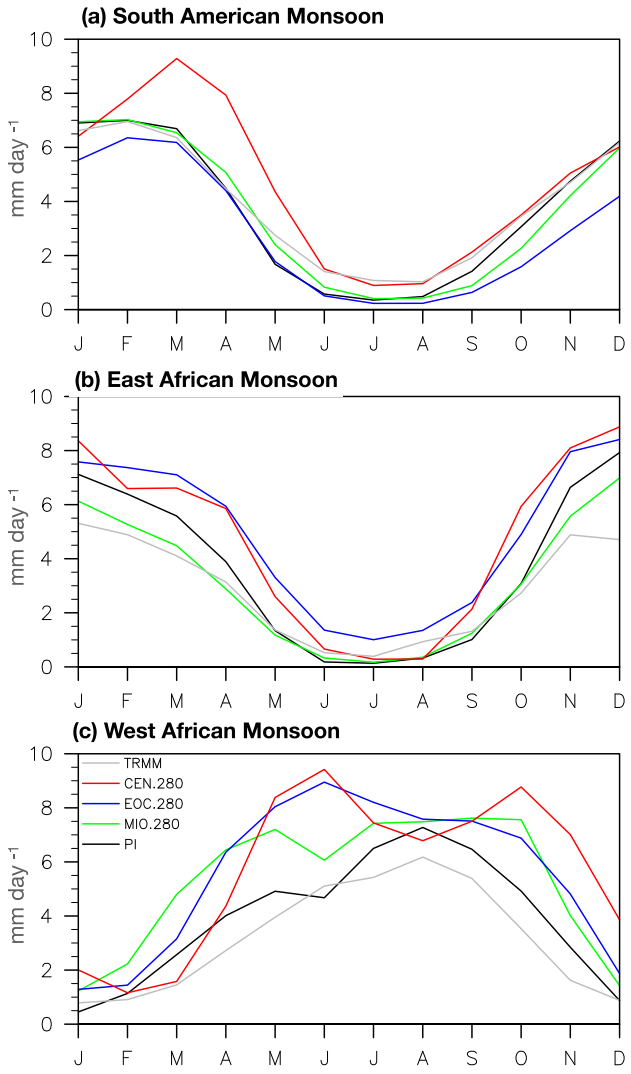

Figure 3. Annual distribution of total precipitation rate (mm day^{-1}) averaged over the monsoon systems found in figure 1. The monsoonal regions are shown in Figures 2f and 2k and are adjusted appropriately for the paleoclimate simulations.

3.3 Role of continental drift on the development of tropical precipitation

3.3.1 Development of the Atlantic Intertropical Convergence Zone

To understand the impact of paleogeography on the development of the Atlantic ITCZ, we examine the evolution of the Hadley cell over the Atlantic region. The region of maximum vertical velocities aligns with the region of maximum subcloud θ_e, upper-level θ_e, diabatic heating, and precipitation rate, which represents the ascending branch of the Hadley cell circulation (Fig. 4). In the PI case, annual surface temperature and precipitation peaks near the equatorial Atlantic (Fig. 4a). The PI simulation shows two axisymmetric overturning circulations

with maximum annual θ_e and diabatic heating at the center. Spatially, the maximum annual subcloud and upper-level θ_e are located over central South America and Africa but expand across the tropical Atlantic Ocean (Fig. S3).

Changes in South Atlantic Basin width cause the regional surface and atmospheric thermodynamic profile and overturning circulation to differ. In the near absence of a South Atlantic Basin, the CEN.280 case exhibits a strong Northern Hemisphere overturning circulation with maximum subcloud, upper-level θ_e, and diabatic heating collocated with the ascending branch of the Hadley cell (~5°N) (Fig. 4d). The Southern Hemisphere overturning circulation, a feature of the modern-day Atlantic ITCZ, is not present in the CEN.280 simulation (Fig. 4d). In this case, the South American and African continents have enhanced subcloud θ_e over the west coast of South America and Africa (Fig. S3), which divert precipitation toward the interior of the continents rather than over the Atlantic Ocean (Fig 2e). In the EOC.280 simulation, southerly low-level winds associated with weak Southern Hemisphere trade winds (Fig. S7) begin to converge toward the region of maximum subcloud, upper-level θ_e, and diabatic heating located north of the equator at ~5°N (Fig. 4c). Additionally, a shallow overturning circulation at ~1°N (Fig. 4c) and weak precipitation (Fig. 2d) over the ocean appear in the EOC.280 simulation. As the South Atlantic Basin nears its modern-day width (MIO.280), the maximum subcloud and upper-level θ_e are spread across both hemispheres with maximum precipitation, diabatic heating, and vertical velocities located along the equator (Fig. 4a and 4b). Notably, a shallow (1000-500 mb) overturning circulation at ~7°S, separate from the large-scale subsidence at ~20°S, forms in the Southern Hemisphere. As in the PI, the MIO.280 simulation shows the formation of Southern Hemisphere trade winds (Fig. S7) and the maximum annual precipitation rates occurring between 5°S and 5°N (Fig. 4b, blue line).

Our simulations indicate that basin width substantially controls the origin and development of the Atlantic ITCZ. The insufficient body of water found over the South Atlantic Basin during the Cenomanian inhibits the formation of a Southern Hemisphere overturning circulation. The substantially closer South American and African continents concentrate the annual mean precipitation toward the continental interior rather than over the ocean. Although the exact period is unknown, the early Eocene represents a transition scenario between the modern-day and the Cenomanian. In this case, the South Atlantic Basin was still narrow but had sufficient fetch for southerly low-level winds and convection to occur over the Atlantic Ocean.

We find the Northern Hemisphere overturning circulation persisting since the formation of the Northern Atlantic Basin (Poblete et al., 2021; Seton et al., 2012). Our study demonstrates that a Southern Hemisphere Hadley cell overturning circulation fully existed in the Miocene, but we hypothesize that this could have occurred earlier as the South Atlantic Basin gained a sufficient fetch (Poblete et al., 2021; Seton et al., 2012).

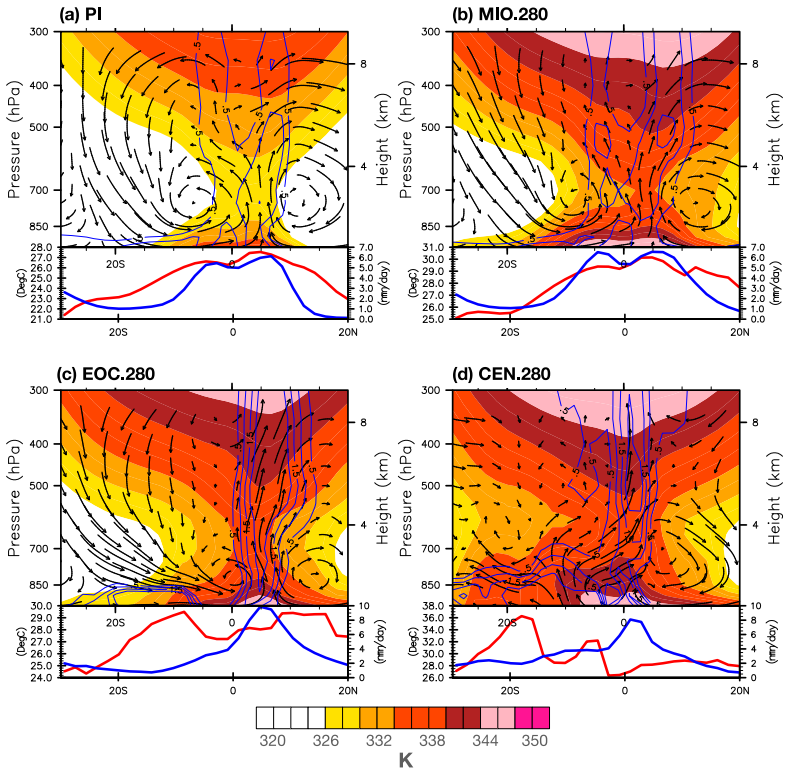

Figure 4. Annual zonal average θ_e (K; color shadings) in pressure coordinates overlain with maximum total diabatic heating (K day^{-1}; light-blue contours lines) in pressure coordinates. Vectors are omega (Pa day^{-1}) scaled with meridional winds (m s^{-1}) with the reference vector of 1. The attached plots show zonal average surface temperature (K, red line) and total precipitation rate (mm/day, blue line). All variables were averaged over 15°W and 30°W. The simulations presented are PI, MIO.280, EOC.280, and CEN.280.

3.3.2 Development of the South American Monsoon

In this section, we identify the role of widening the South Atlantic Basin and the northward movement of South America in the development of the South American monsoon. In the CEN.280 and EOC.280 simulations, maximum subcloud θ_e that is coupled to the upper-level θ_e is isolated over western South America, which leads to a concentration of total precipitable water

over this region (Fig. 5c, 5d, 6c, and 6d). In the EOC.280 simulation, the maximum subcloud θ_e over western South America does not connect with the subcloud θ_e over the equatorial Atlantic Basin, which is supported by the lack of diabatic and precipitable water over the northeastern coast of South America (Fig. 5c, 5d, 6c, and 6d). With the widening of the South Atlantic Basin, the MIO.280 and PI simulations exhibit enhanced subcloud and upper-level θ_e that coincide with enhanced diabatic heating and precipitable water extending from western South America, across the Amazon Basin and terminating at the northeastern coastal region of South American (Fig. 5a, 5b, 6a, and 6b). In sum, the simulations suggest that the widening of the Atlantic results in South American monsoon precipitation expansion over the east Amazon basin.

To explain how paleogeography impacts the formation of convective systems over the Amazon Basin, we show atmospheric moisture flux, SSTs, and currents distribution. In the CEN.280, easterly winds entering South America are weak. Instead, a westerly flow from the Pacific Basin supplies moisture toward western South America (Fig. 6a versus 6d and S6). In the EOC.280, low-level winds and maximum moisture flux originate from northeasterly flow, suggesting a transition to a modern-like surface wind or trade winds-like distribution. Further widening of the South Atlantic Basin and northward migration of the South American continent in the MIO.280 strengthens easterly moisture flux to the continental interior. A full Atlantic easterly trade wind is established in the MIO.280 simulation (Fig. S7). Moisture flux analysis suggests that the additional fetch over the Atlantic Basin and northward location of the South American continent increased the amount of moisture transported into the continental interior (Fig. 6c versus 6b; *Liu et al.* 2019).

Changes in regional ocean circulation due to paleogeography also impacted the South American monsoon. As in World Ocean Atlas (WOA), the PI shows warm SSTs along the tropical west coast of Africa and the tropical eastern coast of South America. In the CEN.280 case, South Atlantic Basin SSTs are substantially warmer than the modern and paleoclimate cases due to the narrowness and shallowness of the basin (Fig. 7e). In the EOC.280 case, warm SSTs form over the tropical west coast of Africa. However, due to the weaker Southern Hemisphere easterly trade winds (Fig. 7d and S7), warm SSTs over the tropical eastern coast of South America do not form. Since the Southern Hemisphere easterly trade winds are fully developed in the MIO.280 case, warm SSTs over the northeastern coast of South America begin to form (Fig. 7b, 7c, and S7). The formation of warm SSTs found over the eastern coast of South

America in the MIO.280 and PI simulations coincide with enhanced easterly moisture flux, the maximum subcloud and upper-level θ_e, and diabatic heating (Fig. 5a, 5b, 7b, and 7c). The coevolution of warm SSTs and convective systems over the northeastern coast of South America suggests that well-developed easterly trade winds, which are not found in the Cenomanian and early Eocene cases when the basin was narrow, are necessary for the South American monsoon precipitation to migrate eastward.

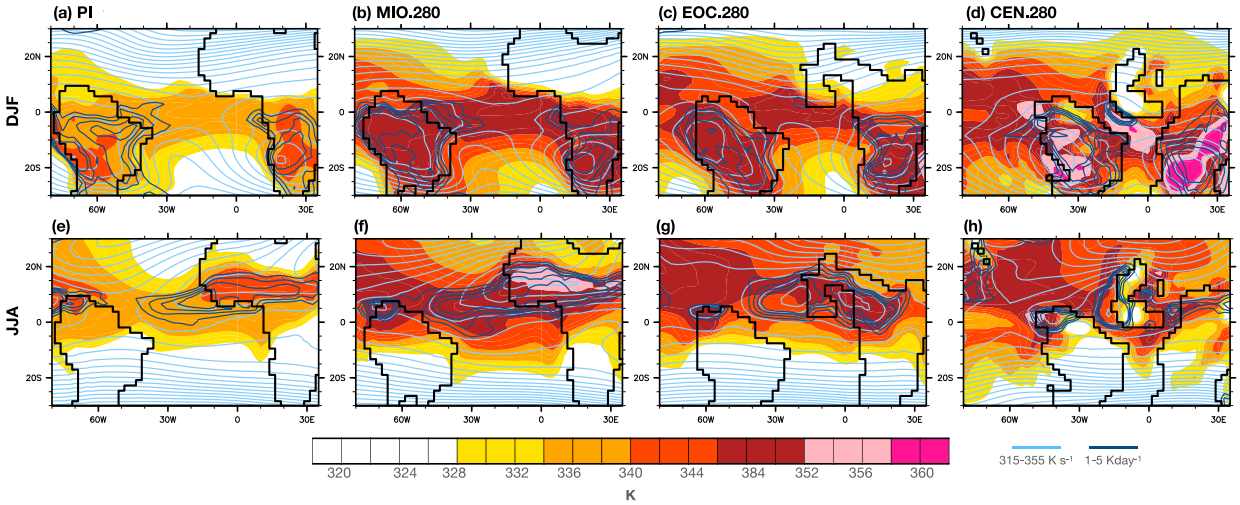

Figure 5. Average subcloud θ_e (850 mb) (K; color shadings) in terrain-following coordinates overlain with upper-level θ_e (315-355K; 200 mb; light blue contours lines) and maximum total diabatic heating (1000 -100 mb) (1-4 K/day; dark blue contours lines) in pressure coordinates. Plots a-d show austral summer (DJF) climatology, and plots e-h show boreal summer (JJA) climatology. The simulations presented are PI, MIO.280, EOC.280, and CEN.280.

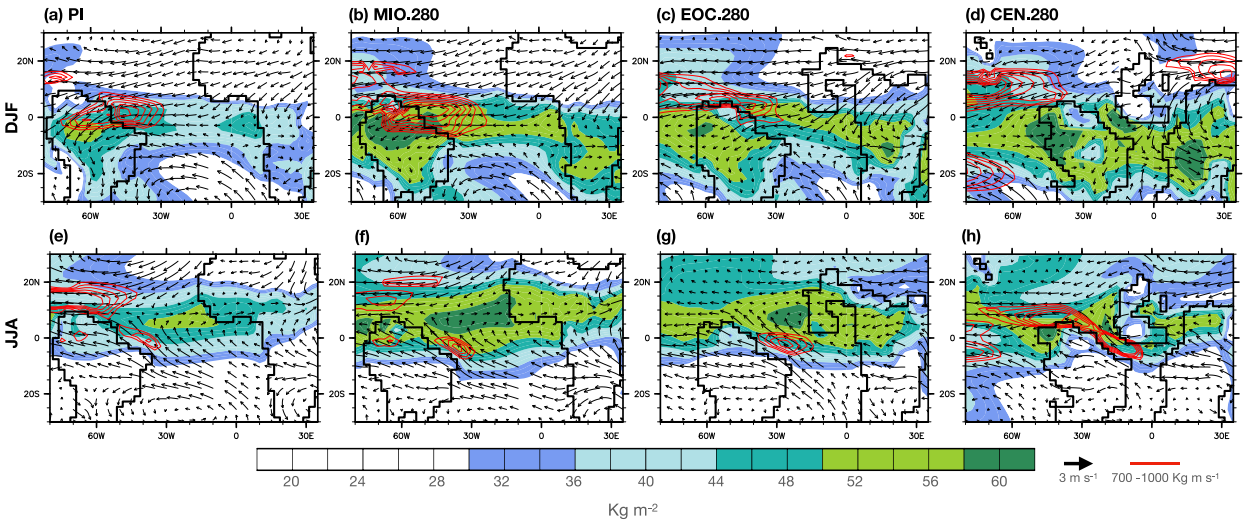

Figure 6. Vertically integrated total precipitable water (kg m^{-2}, color contours), overlain with maximum vertically integrated (1000-100 mb) moisture flux magnitude (kg m s^{-1}, red contour lines) and surface (850 mb) winds (m s^{-1}, vectors) in pressure coordinates. Plots a-d show austral summer (DJF) climatology and plots e-h show boreal summer (JJA) climatology. The simulations presented are PI, MIO.280, EOC.280, and CEN.280.

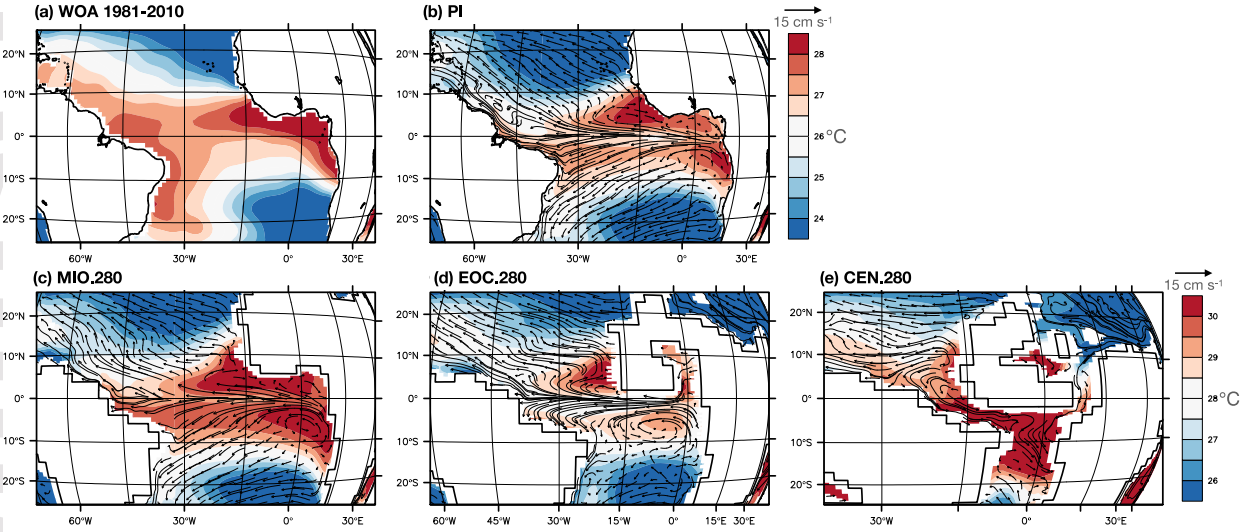

Figure 7. Austral summer (DJF) sea surface temperatures (°C) overlain with surface currents (cm s^{-1}). Plots show the World Ocean Atlas 2018, Boyer et al.,2018 averaged over 1981-2010 (a), and CESM1.2 simulations: PI (b), MIO.280 (c), EOC.280 (c), and CEN.280 (e). Sea surface temperature values show adjusted values for the modern (a and b) and paleoclimate (c, d, and e) cases.

3.3.3 Development of the East and West African monsoons

In Section 3.2, we showed that the East African monsoon precipitation remains near 15°S in all cases. The maximum East African monsoon subcloud θ_e coupled to the upper-level θ_e is centered at 15° S in all four cases, with the CEN.280 with the warmest subcloud θ_e distribution (Fig. 5). Moisture flux analysis in the CEN.280 and EOC.280 indicates that most of the precipitable water is delivered by westerly onshore flow from the South Atlantic Basin and by northeasterly flow from the Tethys seaway (Fig. 3b, 6c, 6d). In the MIO.280 and PI simulations, with the emergence of the northern African landmass and closure of the Tethys Sea, an increased flux of northerly dry air weakens the East African monsoon, making the South Atlantic Basin the primary source of moisture (Fig. 6a and 6b). Warm SSTs found over the Gulf of Guinea during the austral summer remained stationary since the late Cretaceous (Fig. 6 and 7). Notably, differences in the East African Plateau elevation, which vary dramatically between our

simulations, influence the poleward extent and the magnitude of the East African monsoon precipitation (Section 3.6).

Unlike the East African monsoon, the West African monsoon strength in all four simulations is connected to the location of the western coast of West Africa, which drifted away from the equator and South American continent through time. The maximum West African monsoon subcloud θ_e coupled to the upper-level θ_e is centered at ~5° N in the CEN.280, ~10° N in the EOC.280, and at ~15° N in the MIO.280 (Fig. 5). Monsoon diagnostics indicate that the West African monsoon center in the CEN.280 and EOC.280 was located near the equator (Fig. 5g and 5h) and drifted toward the subtropics in the MIO.280 case (Fig. 5f). With West Africa closer to the equator in the CEN.280 and EOC.280 cases, warm surface temperatures over land and adjacent bodies of water (not shown) enhance convection over the region (Fig 2n and 2o). Additionally, a narrow South Atlantic Basin in the CEN.280 and EOC.280 allows strong cross-equatorial flow off the coast of South America to directly deliver moisture into the West African monsoon, further strengthening the circulation in these cases (Fig. 6g and 6h). However, the northward movement of Africa in the MIO.280 and PI cases shifted the circulation toward the subtropics, effectively weakening the thermally driven circulation and increasing its seasonality. At the same time, as the South Atlantic Basin widened, the strong southernly cross-equatorial flow is redistributed along the entire tropical Atlantic Basin, decreasing the moisture flux into the West African monsoon circulation (Fig. 6e and 6f). Since much of the Northern Atlantic Basin was already open during the late Cretaceous, our results indicate that changes in ocean circulation due to the North Atlantic Basin had a much smaller influence on the West African monsoon. In support, seasonally warm SSTs coinciding with the West African monsoon precipitation center over the coast of West Africa appear in all cases (10°N) (Fig. 8).

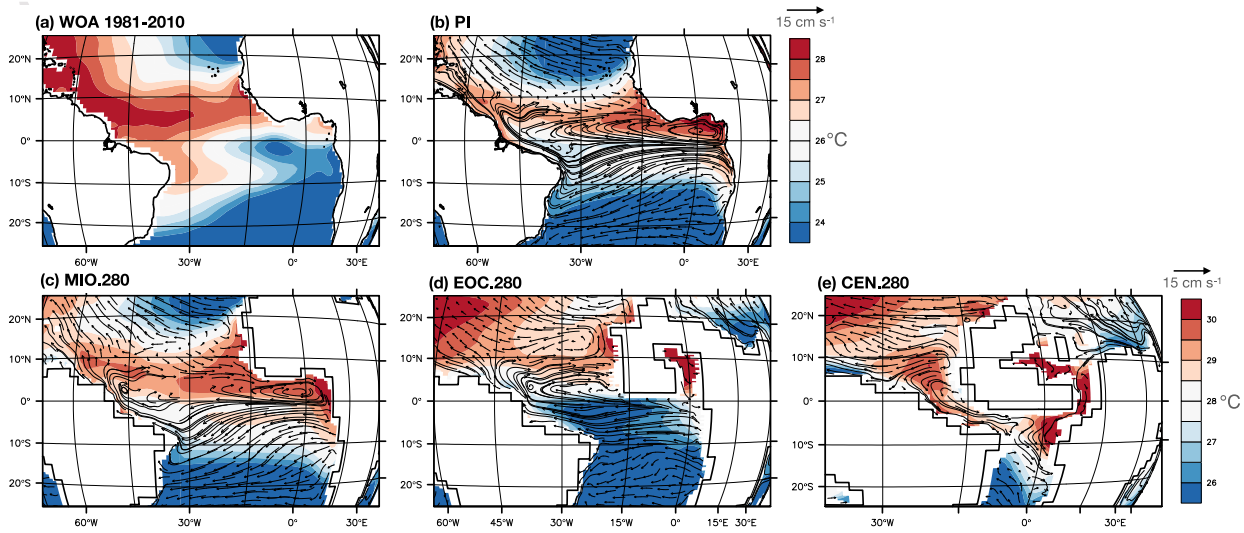

Figure 8. Caption the same as figure 7 but for boreal summer months (JJA).

3.4 Elevated CO_2 levels versus paleogeography

Increasing CO_2 concentrations leads to increased land and ocean surface temperatures in our paleoclimate simulations (Fig. 9 and S8). Increased temperature enhances the already established Atlantic ITCZ, South American, and African monsoon precipitation. We find that increasing CO_2 concentrations do not reorganize precipitation regimes but can primarily strengthen them (Fig. 9 vs. Fig. 1). For example, as in the CEN.280, the monsoon centers remain constant in the CEN.1700 (Fig. 9c, 11f, and 11i). As in the EOC.280, maximum Atlantic ITCZ precipitation is located off the western coast of West Africa in EOC.1700 (Fig. 9b, 9e, and 9h). In MIO.400, the location of the precipitation center for the Atlantic ITCZ, South American, and African monsoons remain the same as we increase CO_2 concentrations (Fig. 9a, 9d, and 9g). Our simulations produce an increased precipitation rate in the subtropics at higher CO_2 levels but only in regions where precipitation is already established.

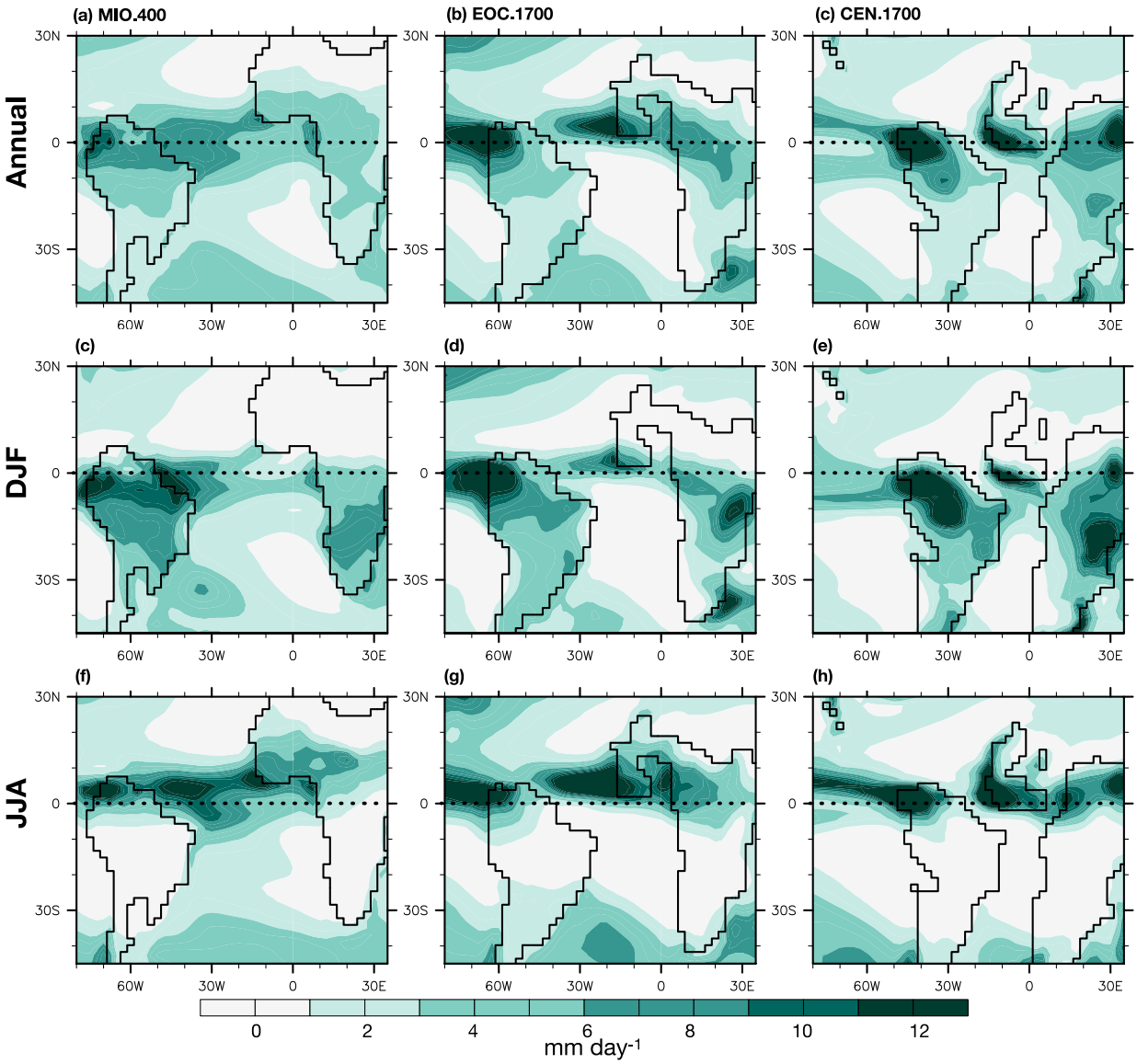

Figure 9. caption same as Figure 2, but for high CO_2 middle Miocene, early Eocene, and Cenomanian cases.

3.5 Topography versus continental drift

To determine if topography strongly impacts the resulting Atlantic ITCZ, South American, and African monsoon precipitation distribution, we provide several topography sensitivity simulations where South America and Africa terrain was flattened. We find that topography enhances tropical precipitation; however, continental drift still has a first-order control on how tropical precipitation is organized. For example, in the CEN.280 case, regions of elevated topographies in northern South America and Africa (Fig. 1d) coincide with the location of

maximum precipitation rates (Fig. 2j). Removal of the high topography lowers the South American monsoon and West African monsoon precipitation over northern South America and Africa but does not remove the associated northwestern South American and African precipitation (Fig. S4c, S4f, S5c, and S5f). Topography, however, influence the poleward organization of precipitation because it can redistribute where the maximum subcloud θ_e and orographic precipitation reside (Fig. 2g and 5a). For example, the Andes topography is low or absent in all the paleoclimate cases. In these cases, southward moisture transport along the Andes, as occurs in the PI via a low-level jet (Insel et al., 2010; Poulsen et al., 2010), is reduced, allowing the maximum subcloud θ_e to be broadly distributed across South America and precipitation is instead focused over northwest South America (Fig. S4). Additionally, flattening the East African Plateau in EOC.280 and CEN.280 disorganizes the East African monsoon precipitation across Central Africa rather than concentrating over the mountains. (Fig. S4c and S4f). The continental distribution strongly controls organized rainfall in the tropics since the regional SST distribution influences the mean zonal wind patterns, but the regional topographies strongly control organized precipitation found in the subtropics since it can redirect the transport of moisture and energy (R. P. Acosta & Huber, 2020; Geen et al., 2020; Lutsko et al., 2019).

3.6 Changes in South American and African Rainforests

By using the KGCC criteria, we characterized the potential spatial extent of the South American and African tropical rainforest, monsoon, and savannah ecosystems through time. We plot the KGCC criteria for the PI case similarly to *Peel et al.* (2007) to validate our CESM1.2 simulations (Figure 10a). The PI case shows the eastern Amazonian rainforest and the equatorial rainforest in Africa (Fig. 10a). The latitudinal extent of the Amazonian monsoon-type rainforest spans from 5°N to 5°S, while the tropical savannah type spans from 10°N to 25°S. Much of the monsoon-type rainforest in Africa is restricted along the equator, while the savannah-type spans from 20°N and 10°S.

The CEN.280 and EOC.280 simulations support the existence of rainforest and monsoon-type ecosystems in northwestern South America and across Central Africa (Fig. 10c and 10d), with their poleward extent increasing when CO_2 levels are raised (Fig. 10f and 10g). Widening the South Atlantic Basin in the MIO.280 simulation leads to an eastward expansion of the Amazon Rainforest (Fig. 10b). A modest increase in CO_2 levels from 280 to 400 ppm during the

middle Miocene does not substantially alter the poleward extent of the Amazon Rainforest (Fig. 10e). The African rainforest and monsoon-type ecosystem in the middle Miocene remain along the equator but are substantially smaller than those found in the CEN.280 and EOC.280, especially when compared to the higher CO_2 cases (Fig. 10e, 10f, and 10g). In all four cases, the savannah ecosystem could have covered much of South America and Africa and expanded poleward with higher CO_2 levels.

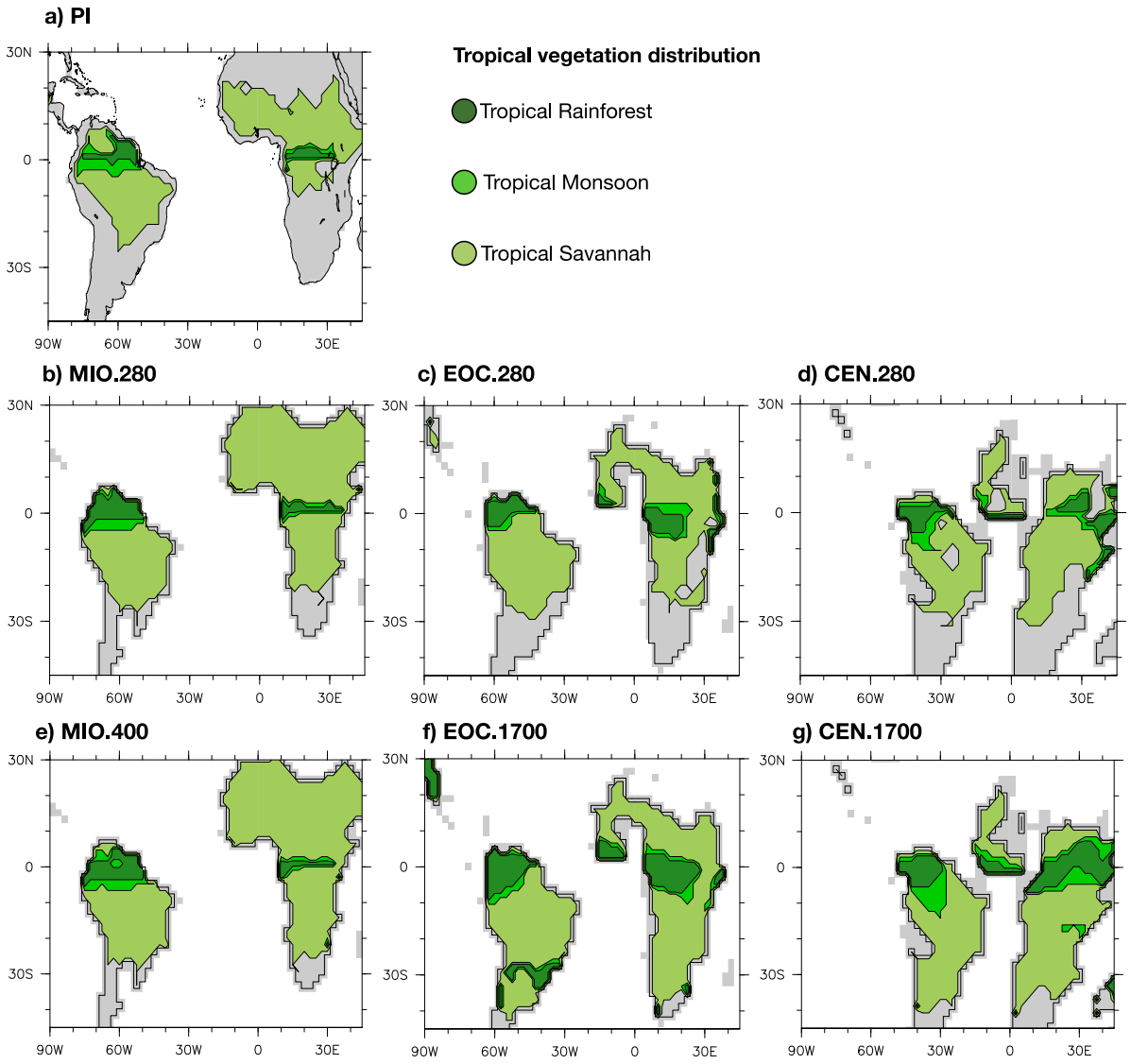

Figure 10. South American and African tropical vegetation distribution was calculated from the Köppen-Geiger climate classification. The simulations presented are PI, MIO.280, EOC.280, CEN.280., MIO.400, EOC.1700, and CEN.1700.

4 Discussion

Our simulations reveal the critical role of South American and African continental drift on the Atlantic ITCZ, South American, and African monsoons. For example, in our Cenomanian simulations when the South Atlantic Basin was narrow, and the South American and African continents were located further south than modern-day, the Southern Hemisphere branch of the Atlantic ITCZ was non-existent or weak since the formation of the Southern Hemisphere overturning circulation was hindered by the lack of ocean surface. However, the breakup of the Gondwana "mega-monsoon" (Kutzbach & Gallimore, 1989; Peyser & Poulsen, 2008) is featured by the Cenomanian simulation where regional South American and African monsoons began development. The early Eocene simulations represent a transitionary period where the South Atlantic Basin had sufficient fetch to allow cross-equatorial flow to enhance the West African monsoon but did not allow strong easterly trade winds during the austral summer months to strengthen the South American monsoon (Liu et al., 2019). The middle Miocene simulations resembled the modern-day since 90% of the South Atlantic Basin was open. In this case, the Atlantic ITCZ and Southern Hemisphere easterly trade winds were fully developed.

Paleotopography impacted the development and location of the South American and African monsoon precipitation centers. For example, the Cenomanian simulations exhibit large terrains over South America and West Africa not present in any other paleo reconstructions. Removal of such high topographies in South America shows the austral summer precipitation center is generally located in the northwestern sector of South America but would be extended southward if the Andes were present (Fig. 1b and S4). We find changes in topography strongly influence local moisture distribution, and the region of maximum subcloud θ_e, which ultimately reorganizes monsoon centers (R. P. Acosta & Huber, 2020; Nie et al., 2010). More recent paleotopographic reconstructions of the Andes suggest that an elevated proto-Andes were already elevated during the Eocene (Boschman, 2021; Canavan et al., 2014; Fiorella et al., 2015), which is not accurately represented in our early Eocene and middle Miocene simulations. Nonetheless, without the elevated Andes, precipitation along the eastern Amazon region occurs in our middle Miocene simulation, suggesting that continental drift, and not the rise of the Andes, was responsible for the eastward expansion of the Amazonian rainforest. However, the poleward extent of the South American monsoon is strongly tied to the presence of the Andes (PI

simulation, Poulsen et al., 2010). We note that the location of the East African Rift Zone, which varied between our simulations, controls the location of maximum austral summer precipitation over Southern Africa. Precipitation becomes less concentrated without the elevated East African Rift Zone (S4). Our work here demonstrates that the uplift of the Andes (Garzione et al., 2017; Poulsen et al., 2010) and the East African Rift Zone (Jung et al., 2016; Wichura et al., 2015) can increase the South American and East African monsoon precipitation magnitude and alter the poleward location of the subtropical monsoon centers; thus an extended focused investigation of the elevated Andes or East African Rift Zone across the Cenozoic should be further tested.

Atmospheric CO_2 concentrations have decreased from well above 1000 ppm in the late Cretaceous to as low as 280 ppm during the preindustrial (Foster et al., 2017), which has substantial implications on the atmospheric hydrological cycle (Natalie J Burls & Fedorov, 2017; Frierson et al., 2007; Held & Soden, 2006; M Huber & Caballero, 2011; Poulsen & Jeffery, 2011; Scheff et al., 2017). Increasing CO_2 is intrinsically tied to the overall warmer land surface and sea surface temperatures. Our simulations show that the elevated atmospheric CO_2 levels during the Cenomanian, early Eocene, and middle Miocene strengthened the Atlantic ITCZ, South American, and African monsoon precipitation rate and moisture flux convergence into the continents (Fig. 9, and S6). However, increasing CO_2 does not substantially modify the locality of the monsoon precipitation centers (Fig. 9). For example, in EOC.1700 simulation, the South American monsoon precipitation found on the northwestern coast was higher than the EOC.280, but the northeastern coast of South America remained relatively dry. Parts of the South American and African subtropics receive more precipitation under warmer climate conditions (N. J Burls & Fedorov, 2017), which is reflected by our KGCC vegetation classification. However, enhanced precipitation rates due to CO_2 only occur in regions where convective systems are already established, which are determined by paleogeography.

We find that large-scale changes in the location of monsoon centers are primarily contingent on the paleogeography, which can change oceanic and atmospheric large-scale circulation (Farnsworth et al., 2019), while fluctuation in CO_2 mainly enhances the already established precipitation centers. We note that due to differences in boundary conditions (paleogeography, vegetation, soil, ice sheet, or aerosol distribution), the 280 ppm CO_2 paleoclimate simulations were warmer than the PI case (Fig. S12a) with the global mean surface temperature (GMST) of the PI, MIO.280, EOC.280, and CEN.280 being ~14, ~19, ~19, and

~20°C, respectively. Such warming due to boundary conditions generally increased zonal mean precipitation rates in the tropics except for the middle Miocene simulation (Fig. S12b). The weaker tropical precipitation rate in the MIO.280 is contrasted by enhanced precipitation in the subtropics suggesting an increase in the export of moisture and energy from the equator toward the poles (not shown). Furthermore, increased CO_2 in the simulations MIO.400, EOC.1700, and CEN.1700 resulted in the global mean surface temperature of ~20, ~30, and ~31°C, respectively. The substantially warmer global mean surface temperature in the CEN.1700 and EOC.1700 cases increase precipitation in the tropics suggesting a more enhanced ITCZ during the late Cretaceous and early Cenozoic versus the late Cenozoic where precipitation is greater in the subtropical monsoon regions (Fig. S12b).

Our results demonstrate that the influence of continental drift was complex and had a substantial impact on the atmospheric and oceanic circulation. For example, the widening of the South Atlantic Basin not only enhances the onshore moisture flux (Liu et al., 2019) but also forms warm SSTs over the northeastern coastal region of South America. Enhanced moisture flux and warm coastal SSTs coincide with enhanced precipitation over the Amazon Basin. Early Eocene SST sensitivity experiment shows that intense northeastern Amazonian precipitation rates can be reproduced without the enhanced increased onshore moisture flux, given that warm coastal SSTs are present (Fig. S9), which naturally occurs with continental drift. Such a simple SST sensitivity test presented here further emphasizes the role of ocean-atmosphere interactions in controlling the various monsoon circulation (R. P. Acosta & Huber, 2020; Lutsko et al., 2019). Additionally, changes in global ocean circulation due to increased CO_2 levels such as the variability in the Atlantic meridional overturning circulation strength (Lynch-Stieglitz, 2017), El Niño-Southern Oscillation (Goldner et al., 2011), and Atlantic upwelling regions (Richter & Xie, 2008) represent avenues that require further investigation. As shown here, the distribution of tropical Atlantic SSTs is essential to the formation of the Atlantic ITCZ (Fig. 7 and 8); thus, changes in AMOC circulation, which is known for transporting heat away from the equator, should be further tested but is beyond the scope of our work.

Using the KGCC criteria, we demonstrate that changes in tropical monsoon strength through time most likely altered the vegetation distribution over South America and Africa. The enhancement of the West African monsoon during the Cenomanian to the early Eocene supports the existence of a thriving Pan-African rainforest. However, the South American monsoon was

restricted toward the northwestern corner of South America (Jaramillo et al., 2010), effectively drying the eastern Amazonian region (Fig. 10f and 10g). As the South Atlantic Basin widened, the South American monsoon began to extend eastward and aided in the west-to-east expansion of the Amazon Forest during the Neogene (Fig. 10a, 10b, and 10e). Weakening of the West African monsoon circulation over time leads to a decreased African rainforest extent. The changes in South American and African monsoon strength and locality over time bolster the hypothesis that the decline of the Pan-African rainforests coincided with the growth of the Amazonian rainforests during the Neogene (Jaramillo et al., 2010; Morley, 2011). We demonstrate that the decline of the African rainforest was due to paleogeography and Cenozoic-CO_2 decline. In contrast, the primary mechanism controlling the Amazon rainforest's eastward expansion was paleogeography rather than CO_2 (Liu et al., 2019). We note that the KGCC criteria are calibrated for modern-day vegetation, and plant adaptations could have substantially differed in the past, allowing them to exist in different environments (Carvalho et al., 2021; Morley, 2011). For example, the KGCC criteria only consider T_{cold} and do not consider an upper bound in surface temperatures (Sullivan et al., 2020), which can reach as warm as ~50°C mean annual temperature in both EOC.1700 and CEN.1700 cases. The addition of paleo plant (Richey et al., 2021) functional types and a dynamic vegetation module (Fisher et al., 2015) in future climate model iterations should further improve the work presented here. Nonetheless, although vegetation in our original paleoclimate simulations is fixed, changing the vegetation in our simulations (Fig. S10 and S11) only increases the precipitation magnitude but does not modify the monsoon precipitation centers suggesting that the hydroclimate is primarily controlled by the continental configuration, regional topography, and CO_2 rather than the already established vegetation.

5 Summary

This study presents paleoclimate simulations of the Cenomanian (~95 Ma), early Eocene (~55 Ma), middle Miocene (~15 Ma), and preindustrial (modern-day) using the Community Earth System Model version 1.2 (CESM1.2). We demonstrated that changes in paleogeography associated with the widening of the South Atlantic Basin, northward movement of the South American and African continents, and uplift of the Andes and East African rift zone altered the Atlantic ITCZ, South American, and African monsoons. Our results indicate that changes in CO_2

levels and vegetation distribution play a secondary role to paleogeography. Lastly, using simple precipitation-temperature criteria, our work demonstrates that a western Amazonian and Pan-African rainforest thrived during the late Cretaceous and early Cenozoic. Changes in paleogeography (widening of the South Atlantic Basin and uplift of various mountain ranges) and CO_2 level decline in the late Cenozoic resulted in the contraction of the Pan-African rainforest and an expansion of the Amazon rainforest.

Acknowledgment

We are grateful to the National Science Foundation Grant (EAR-1550134), the Heising-Simons Foundation (HSF #2016-05, #2016-12), and the University of Michigan for funding our study. We appreciate CISL Data Support Section at NCAR (NSFEAR114504) for providing TRMM climatologies, Mathew Rothstein at NCAR PaleoResource for technical support, and Susan Borda at the University of Michigan Deep Blue for aiding with data archiving. For the helpful insights during the production of our simulations, we thank Nicholas Herold, Matthew Huber, and Clay Tabor. For the valuable discussion and comments during the preparation of the manuscripts, we thank the member of the Michigan paleoclimate research group, Alex Farnsworth, and the reviewer and editor at Paleoceanography and Paleoclimatology. The authors declare no conflict of interest.

Open Research

Datasets for this research are found at the University of Michigan, Deep Blue Repositories (R. Paul Acosta, 2021). The datasets are available in NetCDF format.

References

Acosta, R. P., & Huber, M. (2020). Competing Topographic Mechanisms for the Summer Indo-Asian Monsoon. *Geophysical Research Letters*, *47*(3). https://doi.org/10.1029/2019GL085112

Acosta, R. Paul. (2021). Paleoclimate simulations of the middle Miocene, early Eocene, and Cenomanian [Data set]. University of Michigan Deep Blue Data. Retrieved from https://doi.org/10.7302/6q48-dk51

Anagnostou, E., John, E. H., Edgar, K. M., Foster, G. L., Ridgwell, A., Inglis, G. N., et al. (2016). Changing atmospheric CO2 concentration was the primary driver of early Cenozoic climate. *Nature*, *533*(7603), 380–384. https://doi.org/10.1038/nature17423

Battisti, D. S., Vimont, D. J., & Kirtman, B. P. (2018). 100 Years of Progress in Understanding the Dynamics of Coupled Atmosphere–Ocean Variability. *Meteorological Monographs*, *59*, 8.1-8.57. https://doi.org/10.1175/AMSMONOGRAPHS-D-18-0025.1

Beerling, D. J., & Royer, D. L. (2011). Convergent Cenozoic CO2 history. *Nature Geoscience*, *4*(7), 418–420. https://doi.org/10.1038/ngeo1186

Boschman, L. M. (2021). Andean mountain building since the Late Cretaceous: A paleoelevation reconstruction. *Earth-Science Reviews*, *220*, 103640. https://doi.org/10.1016/j.earscirev.2021.103640

Burls, N. J., Bradshaw, C. D., De Boer, A. M., Herold, N., Huber, M., Pound, M., et al. (2021). Simulating Miocene warmth: insights from an opportunistic Multi- Model ensemble (MioMIP1). *Paleoceanography and Paleoclimatology*. https://doi.org/10.1029/2020pa004054

Burls, Natalie J, & Fedorov, A. V. (2017). Wetter subtropics in a warmer world: Contrasting past and future hydrological cycles. *Proceedings of the National Academy of Sciences of the United States of America*, *114*(49), 12888–12893. https://doi.org/10.1073/pnas.1703421114

Bush, A. B. G., & Philander, S. G. H. (1997). The Late Cretaceous: Simulation with a coupled atmosphere-ocean general circulation model. *Paleoceanography*, *12*(3), 495–516. https://doi.org/10.1029/97PA00721

Canavan, R. R., Carrapa, B., Clementz, M. T., Quade, J., DeCelles, P. G., & Schoenbohm, L. M. (2014). Early cenozoic uplift of the Puna plateau, central andes, based on stable isotope

paleoaltimetry of hydrated volcanic glass. *Geology*, *42*(5), 447–450. https://doi.org/10.1130/G35239.1

Carmichael, M. J., Lunt, D. J., Huber, M., Heinemann, M., Kiehl, J., LeGrande, A., et al. (2016). A model-model and data-model comparison for the early Eocene hydrological cycle. *Climate of the Past*, *12*(2), 455–481. https://doi.org/10.5194/cp-12-455-2016

Carrapa, B., Clementz, M., & Feng, R. (2019). Ecological and hydroclimate responses to strengthening of the Hadley circulation in South America during the Late Miocene cooling. *Proceedings of the National Academy of Sciences of the United States of America*, *116*(20), 9747–9752. https://doi.org/10.1073/pnas.1810721116

Carvalho, M. R., Jaramillo, C., de la Parra, F., Caballero-Rodriguez, D., Herrera, F., Wing, S., et al. (2021). Extinction at the end-Cretaceous and the origin of modern Neotropical rainforest. *Science*, *68*(April), 63–68. https://doi.org/DOI: 10.1126/science.abf1969

Couvreur, T. L. P., Dauby, G., Blach-Overgaard, A., Deblauwe, V., Dessein, S., Droissart, V., et al. (2021). Tectonics, climate and the diversification of the tropical African terrestrial flora and fauna. *Biological Reviews*, *96*(1), 16–51. https://doi.org/10.1111/brv.12644

Cruz, F. W., Vuille, M., Burns, S. J., Wang, X., Cheng, H., Werner, M., et al. (2009). Orbitally driven east–west antiphasing of South American precipitation. *Nature Geoscience*, *2*(3), 210–214. https://doi.org/10.1038/ngeo444

Danabasoglu, G., Bates, S. C., Briegleb, B. P., Jayne, S. R., Jochum, M., Large, W. G., et al. (2012). The CCSM4 ocean component. *Journal of Climate*, *25*(5), 1361–1389. https://doi.org/10.1175/JCLI-D-11-00091.1

Farnsworth, A., White, E., Charles J.R., W., Black, E., & Kniveton, D. R. (2011). Understanding the large scale driving mechanisms of rainfall variability over Central Africa. In *In African Climate and Climate Change* (pp. 101–122). Springer.

Farnsworth, A., Lunt, D., Robinson, S., Valdes, P., Roberts, W., Clift, P., et al. (2019). Past East Asian monsoon evolution controlled by palaeogeography, not CO2. *Science Advances*, (October), 1–14.

Fiorella, R. P., Poulsen, C. J., Pillco Zolá, R. S., Jeffery, M. L., & Ehlers, T. A. (2015). Modern and long-term evaporation of central Andes surface waters suggests paleo archives underestimate Neogene elevations. *Earth and Planetary Science Letters*, *432*, 59–72. https://doi.org/10.1016/j.epsl.2015.09.045

Fisher, R. A., Muszala, S., Verteinstein, M., Lawrence, P., Xu, C., McDowell, N. G., et al. (2015). Taking off the training wheels: The properties of a dynamic vegetation model without climate envelopes, CLM4.5(ED). *Geoscientific Model Development*, *8*(11), 3593–3619. https://doi.org/10.5194/gmd-8-3593-2015

Foster, G. L., Royer, D. L., & Lunt, D. J. (2017). Future climate forcing potentially without precedent in the last 420 million years. *Nature Communications*, *8*, 1–8. https://doi.org/10.1038/ncomms14845

Frierson, D. M. W., Lu, J., & Chen, G. (2007). Width of the Hadley cell in simple and comprehensive general circulation models. *Geophysical Research Letters*, *34*(18), 1–5. https://doi.org/10.1029/2007GL031115

Gadgil, S. (2018). The monsoon system: Land–sea breeze or the ITCZ? *Journal of Earth System Science*, *127*(1), 1–29. https://doi.org/10.1007/s12040-017-0916-x

Garzione, C. N., McQuarrie, N., Perez, N. D., Ehlers, T. A., Beck, S. L., Kar, N., et al. (2017). Tectonic Evolution of the Central Andean Plateau and Implications for the Growth of Plateaus. *Annual Review of Earth and Planetary Sciences*, *45*(1), 529–559. https://doi.org/10.1146/annurev-earth-063016-020612

Gaskell, D. E., Huber, M., O'Brien, C. L., Inglis, G. N., Acosta, R. P., Poulsen, C. J., & Hull, P. M. (2022). The latitudinal temperature gradient and its climate dependence as inferred from foraminiferal δ18O over the past 95 million years. *Proceedings of the National Academy of Sciences*, *119*(11), 1–8. https://doi.org/10.1073/pnas.2111332119/-/DCSupplemental.Published

Geen, R., Bordoni, S., Battisti, D. S., & Hui, K. (2020). Monsoons, ITCZs and the Concept of the Global Monsoon. *Reviews of Geophysics*, 1–45. https://doi.org/10.1029/2020rg000700

Gill, A. E. (1980). Some simple solutions for heat-induced tropical circulation. *Quarterly Journal of the Royal Meteorological Society*, *106*(449), 447–462. https://doi.org/10.1002/qj.49710644905

Goldner, a., Huber, M., Diffenbaugh, N., & Caballero, R. (2011). Implications of the permanent El Niño teleconnection "blueprint" for past global and North American hydroclimatology. *Climate of the Past*, *7*(3), 723–743. https://doi.org/10.5194/cp-7-723-2011

Goldner, A., Huber, M., & Caballero, R. (2013). Does Antarctic glaciation cool the world? *Climate of the Past*, *9*(1), 173–189. https://doi.org/10.5194/cp-9-173-2013

Goldner, A., Herold, N., & Huber, M. (2014). The challenge of simulating the warmth of the mid-Miocene climatic optimum in CESM1. *Climate of the Past*, *10*(2), 523–536. Retrieved from http://www.clim-past.net/10/523/2014/

Heavens, N. G., Shields, C. A., & Mahowald, N. M. (2012). A paleogeographic approach to aerosol prescription in simulations of deep time climate. *Journal of Advances in Modeling Earth Systems*, *4*(11), 1–13. https://doi.org/10.1029/2012MS000166

Held, I. M., & Soden, B. J. (2006). Robust Responses of the Hydrological Cycle to Global Warming. *Journal of Climate*, *19*, 5686–5699.

Herold, N., Müller, R. D., & Seton, M. (2010). Comparing early to middle Miocene terrestrial climate simulations with geological data. *Geosphere*, *6*(6), 952–961. https://doi.org/10.1130/ges00544.1

Herold, N., Huber, M., & Müller, R. D. (2011). Modeling the Miocene Climatic Optimum. Part I: Land and Atmosphere*. *Journal of Climate*, *24*(24), 6353–6372. https://doi.org/10.1175/2011jcli4035.1

Herold, N., Buzan, J., Seton, M., Goldner, A., Green, J. A. M., Müller, R. D., et al. (2014). A suite of early Eocene (~ 55 Ma) climate model boundary conditions. *Geoscientific Model Development*, *7*(5), 2077–2090. https://doi.org/10.5194/gmd-7-2077-2014

Hoorn, C., Wesselingh, F. P., Steege, H., Bermudez, M. A., Mora, A., Sevink, J., et al. (2010). Amazonia Through Time : Andean Uplift, Climate Change, Landscape Evolution, and Biodiversity. *Science*, *330*, 927–932.

Huber, M, & Caballero, R. (2011). The early Eocene equable climate problem revisited. *Climate of the Past*, *7*(2), 603–633.

Huber, Matthew, & Goldner, A. (2012). Eocene monsoons. *Journal of Asian Earth Sciences*, *44*, 3–23. Retrieved from http://linkinghub.elsevier.com/retrieve/pii/S1367912011003725

Huffman, G. J., Bolvin, D. T., Nelkin, E. J., Wolff, D. B., Adler, R. F., Gu, G., et al. (2007). The TRMM Multisatellite Precipitation Analysis (TMPA): Quasi-Global, Multiyear, Combined-Sensor Precipitation Estimates at Fine Scales. *Journal of Hydrometeorology*, *8*, 38–55.

Hunke, E. C. (2010). Thickness sensitivities in the CICE sea ice model. *Ocean Modelling*, *34*(3–4), 137–149. https://doi.org/10.1016/j.ocemod.2010.05.004

Jaramillo, C., Hoorn, C., Silva, S. A. F., Leite, F., Herrera, F., Quiroz, L., et al. (2010). The Origin of the Modern Amazon Rainforest: Implications of the Palynological and

Palaeobotanical Record. *Amazonia, Landscape and Species Evolution: A Look into the Past*, 317–334. https://doi.org/10.1002/9781444306408.ch19

Jess, S., Koehn, D., Fox, M., Enkelmann, E., Sachau, T., & Aanyu, K. (2020). Paleogene initiation of the Western Branch of the East African Rift: The uplift history of the Rwenzori Mountains, Western Uganda. *Earth and Planetary Science Letters*, *552*, 116593. https://doi.org/10.1016/j.epsl.2020.116593

Jung, G., Prange, M., & Schulz, M. (2016). Influence of topography on tropical African vegetation coverage. *Climate Dynamics*, *46*(7–8), 2535–2549. https://doi.org/10.1007/s00382-015-2716-9

Kutzbach, J. E., & Gallimore, R. G. (1989). Pangaean climates: megamonsoons of the megacontinent. *Journal of Geophysical Research*, *94*(D3), 3341–3357. https://doi.org/10.1029/JD094iD03p03341

Ladant, J. B., Poulsen, C. J., Fluteau, F., Tabor, C. R., Macleod, K. G., Martin, E. E., et al. (2020). Paleogeographic controls on the evolution of Late Cretaceous ocean circulation. *Climate of the Past*, *16*(3), 973–1006. https://doi.org/10.5194/cp-16-973-2020

Laugié, M., Donnadieu, Y., Ladant, J. B., Mattias Green, J. A., Bopp, L., & Raisson, F. (2020). Stripping back the modern to reveal the Cenomanian-Turonian climate and temperature gradient underneath. *Climate of the Past*, *16*(3), 953–971. https://doi.org/10.5194/cp-16-953-2020

Linder, H. Peter. (2014). The evolution of African plant diversity. *Frontiers in Ecology and Evolution*, *2*(JUL), 1–14. https://doi.org/10.3389/fevo.2014.00038

Linder, Hans Peter. (2017). East African Cenozoic vegetation history. *Evolutionary Anthropology*, *26*(6), 300–312. https://doi.org/10.1002/evan.21570

Liu, X., Battisti, D. S., White, R. H., & Baker, P. A. (2019). South American Climate during the Early Eocene: Impact of a Narrower Atlantic and Higher Atmospheric CO2. *Journal of Climate*. https://doi.org/10.1175/JCLI-D-19-0170.1.

Lossada, A. C., Giambiagi, L., Hoke, G. D., Fitzgerald, P. G., Creixell, C., Murillo, I., et al. (2017). Thermochronologic Evidence for Late Eocene Andean Mountain Building at 30°S. *Tectonics*, *36*(11), 2693–2713. https://doi.org/10.1002/2017TC004674

Lundberg, J., Marshall, L. G., Guerrero, J., Horton, B., Malabarba, M. C., & Wesselingh, F. (1998). The Stage for Neotropical Fish Diversification: A History of Tropical South

American Rivers. *Phylogeny and Classification of Neotropical Fishes*, 603.

Lunt, D. J., Farnsworth, A., Loptson, C., L Foster, G., Markwick, P., O'Brien, C. L., et al. (2016). Palaeogeographic controls on climate and proxy interpretation. *Climate of the Past*, *12*(5), 1181–1198. https://doi.org/10.5194/cp-12-1181-2016

Lunt, D. J., Huber, M., Baatsen, M. L. J., Caballero, R., DeConto, R., Donnadieu, Y., et al. (2017). DeepMIP: experimental design for model simulations of the EECO, PETM, and pre-PETM. *Gepscientific Model Development*, 1–16. https://doi.org/10.5194/gmd-2016-127

Lutsko, N. J., Marshall, J., & Green, B. (2019). Modulation of Monsoon Circulations by Cross-Equatorial Ocean Heat Transport. *Journal of Climate*, 3471–3485. https://doi.org/10.1175/jcli-d-18-0623.1

Lynch-Stieglitz, J. (2017). The Atlantic Meridional Overturning Circulation and Abrupt Climate Change. *Annual Review of Marine Science*, *9*(1), 83–104. https://doi.org/10.1146/annurev-marine-010816-060415

Markwick, P. J., & Valdes, P. J. (2004). Palaeo-digital elevation models for use as boundary conditions in coupled ocean–atmosphere GCM experiments: a Maastrichtian (late Cretaceous) example. *Palaeogeography, Palaeoclimatology, Palaeoecology*, *213*(1–2), 37–63. https://doi.org/10.1016/j.palaeo.2004.06.015

Meehl, G. a., Washington, W. M., Arblaster, J. M., Hu, A., Teng, H., Kay, J. E., et al. (2013). Climate Change Projections in CESM1(CAM5) Compared to CCSM4. *Journal of Climate*, *26*(17), 6287–6308. https://doi.org/10.1175/JCLI-D-12-00572.1

Morley, R. J. (2011). Cretaceous and Tertiary climate change and the past distribution of megathermal rainforests. In M. Bush, J. Flenley, & W. Gosling (Eds.), *Tropical Rainforest Responses to Climatic Change* (pp. 1–34). Berlin, Heidelberg: Springer Berlin Heidelberg. https://doi.org/10.1007/978-3-642-05383-2_1

Moulin, M., Aslanian, D., & Unternehr, P. (2010). A new starting point for the South and Equatorial Atlantic Ocean. *Earth-Science Reviews*, *98*(1–2), 1–37. https://doi.org/10.1016/j.earscirev.2009.08.001

Müller, R. D., Sdrolias, M., Gaina, C., & Roest, W. R. (2008). Age, spreading rates, and spreading asymmetry of the world's ocean crust. *Geochemistry, Geophysics, Geosystems*, *9*(4), 1–19. https://doi.org/10.1029/2007GC001743

Neale, R. B., Chen, C., Lauritzen, P. H., Williamson, D. L., Conley, A. J., Smith, A. K., et al.

(2010). Description of the NCAR Community Atmosphere Model (CAM 5.0). *NCAR Tech. Note NCAR/TN-486+ STR*.

Nie, J., Boos, W. R., & Kuang, Z. (2010). Observational evaluation of a convective quasi-equilibrium view of monsoons. *Journal of Climate*, *23*(16), 4416–4428. https://doi.org/10.1175/2010JCLI3505.1

Ogwang, B. A., Chen, H., Li, X., & Gao, C. (2014). The influence of topography on East African October to December climate: Sensitivity experiments with RegCM4. *Advances in Meteorology*, *2014*. https://doi.org/10.1155/2014/143917

Ohba, M., & Ueda, H. (2010). A GCM study on effects of continental drift on tropical climate at the early and late cretaceous. *Journal of the Meteorological Society of Japan*, *88*(6), 869–881. https://doi.org/10.2151/jmsj.2010-601

Oleson, K. W., Lawrence, D. M., Bonan, G. B., Drewniak, B., Huang, M., Koven, C. D., et al. (2013). Technical Description of version 4.5 of the Community Land Model (CLM), (July), NCAR/TN-503+STR. Retrieved from http://www.cesm.ucar.edu/models/cesm1.2/clm/CLM45_Tech_Note.pdf

Peel, M. C., Finlayson, B. L., & McMahon, T. A. (2007). Updated world map of the Köppen-Geiger climate classification. *Hydrology and Earth System Sciences*, *11*(5), 1633–1644. https://doi.org/10.5194/hess-11-1633-2007

Peyser, C. E., & Poulsen, C. J. (2008). Controls on Permo-Carboniferous precipitation over tropical Pangaea: A GCM sensitivity study. *Palaeogeography, Palaeoclimatology, Palaeoecology*, *268*(3–4), 181–192. https://doi.org/10.1016/j.palaeo.2008.03.048

Pletsch, T., Erbacher, J., Holbourn, A. E. L., Kuhnt, W., Moullade, M., Oboh-Ikuenobede, F. E., et al. (2001). Cretaceous separation of Africa and South America: The view from the West African margin (ODP Leg 159). *Journal of South American Earth Sciences*, *14*(2), 147–174. https://doi.org/10.1016/S0895-9811(01)00020-7

Poblete, F., Dupont-Nivet, G., Licht, A., van Hinsbergen, D. J. J., Roperch, P., Mihalynuk, M. G., et al. (2021). Towards interactive global paleogeographic maps, new reconstructions at 60, 40 and 20 Ma. *Earth-Science Reviews*, *214*(January), 103508. https://doi.org/10.1016/j.earscirev.2021.103508

Poulsen, C. J., & Jeffery, M. L. (2011). Climate change imprinting on stable isotopic compositions of high-elevation meteoric water cloaks past surface elevations of major

orogens. *Geology*, *39*(6), 595–598. https://doi.org/10.1130/G32052.1

Poulsen, C. J., Ehlers, T. A., & Insel, N. (2010). Onset of Convective Rainfall During Gradual Late Miocene Rise of the Central Andes, *328*(April), 490–494.

Privé, N. C., & Plumb, R. A. (2007a). Monsoon Dynamics with Interactive Forcing. Part I: Axisymmetric Studies. *Journal of the Atmospheric Sciences*, *64*(5), 1417–1430. https://doi.org/10.1175/JAS3916.1

Privé, N. C., & Plumb, R. A. (2007b). Monsoon Dynamics with Interactive Forcing. Part II: Impact of Eddies and Asymmetric Geometries. *Journal of the Atmospheric Sciences*, *64*(5), 1431–1442. Retrieved from http://journals.ametsoc.org/doi/abs/10.1175/JAS3917.1

Richey, J. D., Montañez, I. P., White, J. D., DiMichele, W. A., Matthaeus, W. J., Poulsen, C. J., et al. (2021). Modeled physiological mechanisms for observed changes in the late Paleozoic plant fossil record. *Palaeogeography, Palaeoclimatology, Palaeoecology*, *562*(September 2020), 110056. https://doi.org/10.1016/j.palaeo.2020.110056

Richter, I., & Xie, S. P. (2008). On the origin of equatorial Atlantic biases in coupled general circulation models. *Climate Dynamics*, *31*(5), 587–598. https://doi.org/10.1007/s00382-008-0364-z

Roberts, E. M., Stevens, N. J., O'Connor, P. M., Dirks, P. H. G. M., Gottfried, M. D., Clyde, W. C., et al. (2012). Initiation of the western branch of the East African Rift coeval with the eastern branch. *Nature Geoscience*, *5*(4), 289–294. https://doi.org/10.1038/ngeo1432

Scheff, J., Seager, R., Liu, H., & Coats, S. (2017). Are glacials dry? Consequences for paleoclimatology and for greenhouse warming. *Journal of Climate*, *30*(17), 6593–6609. https://doi.org/10.1175/JCLI-D-16-0854.1

Sepulchre, P., Ramstein, G., Fluteau, F., Schuster, M., Tiercelin, J., & Brunet, M. (2006). Tectonic Uplift and Eastern Africa Aridification. *Science*, *313*(September), 1419–1423.

Seton, M., Müller, R. D., Zahirovic, S., Gaina, C., Torsvik, T., Shephard, G., et al. (2012). Global continental and ocean basin reconstructions since 200Ma. *Earth-Science Reviews*, *113*(3–4), 212–270. https://doi.org/10.1016/j.earscirev.2012.03.002

Sewall, J. O., Van De Wal, R. S. W., Van Der Zwan, K., Van Oosterhout, C., Dijkstra, H. A., & Scotese, C. R. (2007). Climate model boundary conditions for four Cretaceous time slices. *Climate of the Past*, *3*(4), 647–657. https://doi.org/10.5194/cp-3-647-2007

Singh, H. K. A., Bitz, C. M., & Frierson, D. M. W. (2016). The global climate response to

lowering surface orography of Antarctica and the importance of atmosphere-ocean coupling. *Journal of Climate*, *29*(11), 4137–4153. https://doi.org/10.1175/JCLI-D-15-0442.1

Siongco, A. C., Hohenegger, C., & Stevens, B. (2015). The Atlantic ITCZ bias in CMIP5 models. *Climate Dynamics*, *45*(5–6), 1169–1180. https://doi.org/10.1007/s00382-014-2366-3

Sullivan, M. J. P., Lewis, S. L., Affum-Baffoe, K., Castilho, C., Costa, F., Sanchez, A. C., et al. (2020). Long-term thermal sensitivity of earth's tropical forests. *Science*, *368*(6493), 869–874. https://doi.org/10.1126/science.aaw7578

Tabor, C., Otto-Bliesner, B. L., & Liu, Z. (2020). Speleothems of South American and Asian Monsoons Influenced by a Green Sahara. *Geophysical Research Letters*, *47*(22), 1–11. https://doi.org/10.1029/2020GL089695

Tabor, C. R., Poulsen, C. J., Lunt, D. J., Rosenbloom, N. A., Otto-Bliesner, B. L., Markwick, P. J., et al. (2016). The cause of Late Cretaceous cooling: A multimodel-proxy comparison. *Geology*, *44*(11), 963–966. https://doi.org/10.1130/G38363.1

Tierney, J. E., Poulsen, C. J., Montañez, I. P., Bhattacharya, T., Feng, R., Ford, H. L., et al. (2020). Past climates inform our future. *Science*, *370*(6517). https://doi.org/10.1126/science.aay3701

Wang, B., & Ding, Q. (2006). Changes in global monsoon precipitation over the past 56 years. *Geophysical Research Letters*, *33*(6), L06711. https://doi.org/10.1029/2005GL025347

Wichura, H., Jacobs, L. L., Lin, A., Polcyn, M. J., Manthi, F. K., Winkler, D. A., et al. (2015). A 17-My-old whale constrains onset of uplift and climate change in east Africa. *Proceedings of the National Academy of Sciences of the United States of America*, *112*(13), 3910–3915. https://doi.org/10.1073/pnas.1421502112

Wright, J. S., & Fueglistaler, S. (2013). Large differences in reanalyses of diabatic heating in the tropical upper troposphere and lower stratosphere. *Atmospheric Chemistry and Physics*, *13*, 9565–9576.

Zhu, J., Poulsen, C. J., & Tierney, J. E. (2019). Simulation of Eocene extreme warmth and high climate sensitivity through cloud feedbacks. *Science Advances*, 1–11. https://doi.org/10.1126/sciadv.aax1874

Zhu, J., Poulsen, C. J., Otto-Bliesner, B. L., Liu, Z., Brady, E. C., & Noone, D. (2020).

Simulation of early Eocene water isotopes using an Earth system model and its implication for past climate reconstruction. *Earth and Planetary Science Letters*, *537*. https://doi.org/10.1016/j.epsl.2020.116164

Ziegler, A. M., Eshel, G., McAllister Rees, P., Rothfus, T. A., Rowley, D. B., & Sunderlin, D. (2003). Tracing the tropics across land and sea: Permian to present. *Lethaia*, *36*(3), 227–254. https://doi.org/10.1080/00241160310004657

Boyer, Tim P.; Garcia, Hernan E.; Locarnini, Ricardo A.; Zweng, Melissa M.; Mishonov, Alexey V.; Reagan, James R.; Weathers, Katharine A.; Baranova, Olga K.; Seidov, Dan; Smolyar, Igor V. (2018). World Ocean Atlas 2018. [indicate subset used]. NOAA National Centers for Environmental Information.
Dataset. https://www.ncei.noaa.gov/archive/accession/NCEI-WOA18.